



RESEARCH ARTICLE

10.1002/2015JA021807

Key Points:

- Hot plasma pressure anisotropy current is dominant in the middle magnetosphere
- Shifts main oval and Ganymede footprint from varying hot plasma pressure: comparable to observations
- Middle magnetosphere is near to the firehose stability limit

Correspondence to:

J. D. Nichols,
jdn4@le.ac.uk

Citation:

Nichols, J. D., N. Achilleos, and S. W. H. Cowley (2015), A model of force balance in Jupiter's magnetodisc including hot plasma pressure anisotropy, *J. Geophys. Res. Space Physics*, 120, doi:10.1002/2015JA021807.

Received 13 AUG 2015

Accepted 14 NOV 2015

Accepted article online 18 NOV 2015

A model of force balance in Jupiter's magnetodisc including hot plasma pressure anisotropy

J. D. Nichols¹, N. Achilleos², and S. W. H. Cowley¹
¹Department of Physics and Astronomy, University of Leicester, Leicester, UK, ²Atmospheric Physics Laboratory, University College London, London, UK

Abstract We present an iterative vector potential model of force balance in Jupiter's magnetodisc that includes the effects of hot plasma pressure anisotropy. The fiducial model produces results that are consistent with Galileo magnetic field and plasma data over the whole radial range of the model. The hot plasma pressure gradient and centrifugal forces dominate in the regions inward of $\sim 20 R_J$ and outward of $\sim 50 R_J$, respectively, while for realistic values of the pressure anisotropy, the anisotropy current is either the dominant component or at least comparable with the hot plasma pressure gradient current in the region in between. With the inclusion of hot plasma pressure anisotropy, the $\sim 1.2^\circ$ and $\sim 2.7^\circ$ shifts in the latitudes of the main oval and Ganymede footprint, respectively, associated with variations over the observed range of the hot plasma parameter K_h , which is the product of hot pressure and unit flux tube volume, are comparable to the shifts observed in auroral images. However, the middle magnetosphere is susceptible to the firehose instability, with peak equatorial values of $\beta_{h\parallel e} - \beta_{h\perp e} \simeq 1 - 2$, for $K_h = 2.0 - 2.5 \times 10^7 \text{ Pa m T}^{-1}$. For larger values of K_h , $\beta_{h\parallel e} - \beta_{h\perp e}$ exceeds 2 near $\sim 25 R_J$ and the model does not converge. This suggests that small-scale plasmoid release or "drizzle" of iogenic plasma may often occur in the middle magnetosphere, thus forming a significant mode of plasma mass loss, alongside plasmoids, at Jupiter.

1. Introduction

A characteristic feature of Jupiter's middle magnetosphere is that it is radially distended into a magnetodisc configuration, owing to the existence of a substantial azimuthal equatorial current sheet [e.g., *Khurana et al.*, 2004, and references therein]. The nature of the current sheet at Jupiter is of particular significance for the magnetosphere-ionosphere (M-I) coupling current system, which has received significant attention over recent years, owing to its role in driving the planet's bright main auroral oval emission [*Hill*, 1979, 2001; *Pontius*, 1997; *Cowley and Bunce*, 2001]. In this process, the volcanic moon Io releases $\sim 1000 \text{ kg s}^{-1}$ of sulfur and oxygen into a cloud surrounding the moon. A proportion of this material becomes ionized by electron impact ionization and becomes centrifugally unstable, diffusing radially outward to form an equatorial disk of rotating plasma. Conservation of angular momentum establishes an angular velocity gradient in the plasma that, when mapped along magnetic field lines to the ionosphere, induces an equatorward directed Pedersen current. The azimuthal $\mathbf{J} \times \mathbf{B}$ force associated with this current is mathematically equivalent to the volume force exerted on the neutrals due to collisions with the ions, and the associated torque is communicated to the equatorial plane via the sweep back of field lines out of meridian planes. In the magnetosphere, the $\mathbf{J} \times \mathbf{B}$ associated with the resulting radial current acts to maintain partial corotation at $\sim 50\%$ of the planet's angular velocity out to at least $60 R_J$ [*Kane et al.*, 1995]. The current circuit associated with this M-I coupling system is shown in the schematic in Figure 1, and the upward field-aligned component, carried by downward precipitating electrons, drives the most significant of Jupiter's auroral components, the main oval [*Grodent et al.*, 2003a; *Clarke et al.*, 2004; *Nichols et al.*, 2009]. This current system has been extensively studied recently, in works considering, e.g., the effects of the mass outflow rate \dot{M} and ionospheric Pedersen conductance Σ_p^* [*Nichols and Cowley*, 2003, 2004; *Tao et al.*, 2010], field-aligned voltages [*Nichols and Cowley*, 2005; *Ray et al.*, 2010], and solar wind pressure pulses [*Cowley and Bunce*, 2003; *Cowley et al.*, 2007; *Yates et al.*, 2012].

Although in the above studies of the M-I coupling current system the current sheet magnetic field was treated as a fixed, empirical input to the models, *Cowley et al.* [2002] had shown that the radial stretching of the field in the middle magnetosphere has a profound effect on the location and magnitude of the currents flowing in the

©2015. The Authors.

This is an open access article under the terms of the Creative Commons Attribution License, which permits use, distribution and reproduction in any medium, provided the original work is properly cited.

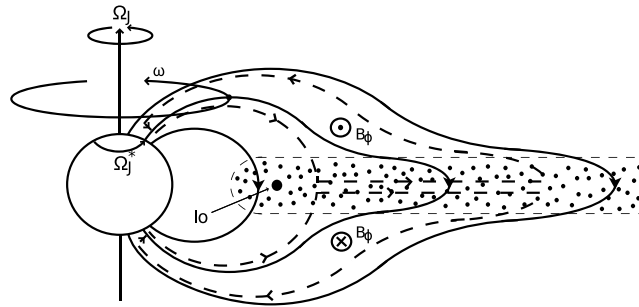


Figure 1. Sketch of a meridian cross section through Jupiter's inner and middle magnetospheres, showing the principal physical features involved. The arrowed solid lines indicate magnetic field lines, the arrowed dashed lines the magnetosphere-ionosphere coupling current system, and the dotted region the rotating disk of outflowing plasma. After Cowley and Bunce [2001].

system through the field line mapping between the equatorial plane and the ionosphere. The current sheet arises since the associated $\mathbf{J} \times \mathbf{B}$ force balances radial centrifugal, pressure gradient, and pressure anisotropy forces that exist in the magnetosphere. In order to include these effects self-consistently in computations of the plasma flow and currents, Nichols [2011, hereafter N11] incorporated the force balance magnetodisc model of Caudal [1986, hereafter C86] (also used by Achilleos *et al.* [2010]) with a focus on application to Saturn). C86's calculations had indicated that hot plasma pressure provides the dominant contribution to the azimuthal current, although N11 showed that use of a more realistic plasma angular velocity profile results in the centrifugal current becoming dominant in the outer magnetosphere. Using this model, N11 also showed that the radial stretching of the field, and thus the magnitude and ionospheric latitude of the auroral currents, is dependent on the ionospheric Pedersen conductance and the iogenic plasma mass outflow rate. The mapping between the equator and ionosphere is of particular interest, since Grodent *et al.* [2008] showed that the ionospheric latitudes of the main oval (mapping to $\sim 20\text{--}30 R_J$) and the Ganymede footprint (mapping to $\sim 15 R_J$) are observed to shift in latitude by up to $\sim 3^\circ$ and $\sim 2^\circ$, respectively, when comparing Hubble Space Telescope (HST) images of Jupiter's ultraviolet auroras that obtained a number of years apart as shown in Figure 2. The change in the Ganymede footprint latitude implicates a change in the magnetodisc current intensity and thus the mapping between ionosphere and equator. However, N11 showed that very large changes in the plasma mass outflow rate, well over an order of magnitude, would be required to reproduce shifts of the magnitude observed by Grodent *et al.* [2008].

A key limitation of the Caudalian model used by N11 is that it assumes that the plasma pressure is isotropic, such that the only outward forces are plasma pressure gradient and the centrifugal force. However, Mauk and Krimigis [1987] have shown using Voyager Low-Energy Charged Particle Instrument energetic (>30 keV) particle data that hot plasma pressure anisotropy is also required in the middle magnetosphere beyond $\sim 22 R_J$ in order to balance the inward $\mathbf{J} \times \mathbf{B}$ force inferred from magnetic data. Indeed, Paranicas *et al.* [1991] later presented three observations of the hot plasma pressure anisotropy from Voyager data obtained during plasma sheet crossings on the nightside and showed that $(p_{\parallel}/p_{\perp}) = 1.06\text{--}1.19$, where p_{\parallel} and p_{\perp} are the components of the plasma pressure parallel and perpendicular to the magnetic field, respectively. Further, Galileo Plasma Science Instrument data indicate that the cold ($\lesssim 1$ keV) plasma exhibits $(p_{\parallel}/p_{\perp}) = 0.2\text{--}1$ inward of $\sim 10 R_J$ [Bagenal, 1994] but that $(p_{\parallel}/p_{\perp})$ increases with equatorial radial distance and that, although it varies significantly, $(p_{\parallel}/p_{\perp})$ is generally >1 at equatorial distances larger than $\sim 25 R_J$ [Frank and Paterson, 2004]. Pressure anisotropy has implications for the current sheet structure and radial force balance, which are not accounted for in the present models of Jupiter's magnetodisc or M-I coupling current system. Briefly, pressure anisotropy acts to change the distribution of azimuthal current density along a field line. Anisotropy with $(p_{\perp} > p_{\parallel})$ spreads the azimuthal current away from the equatorial plane, thickening the current sheet and increasing the radius of curvature of the magnetic field. Conversely, with $(p_{\parallel} > p_{\perp})$, as is the case in Jupiter's middle magnetosphere, the plasma pressure concentrates the azimuthal current in equatorial regions of large field curvature, which is hence accentuated, within the limit of the marginal firehose stability condition (MFC), given by

$$\beta_{\parallel} - \beta_{\perp} < 2, \quad (1)$$

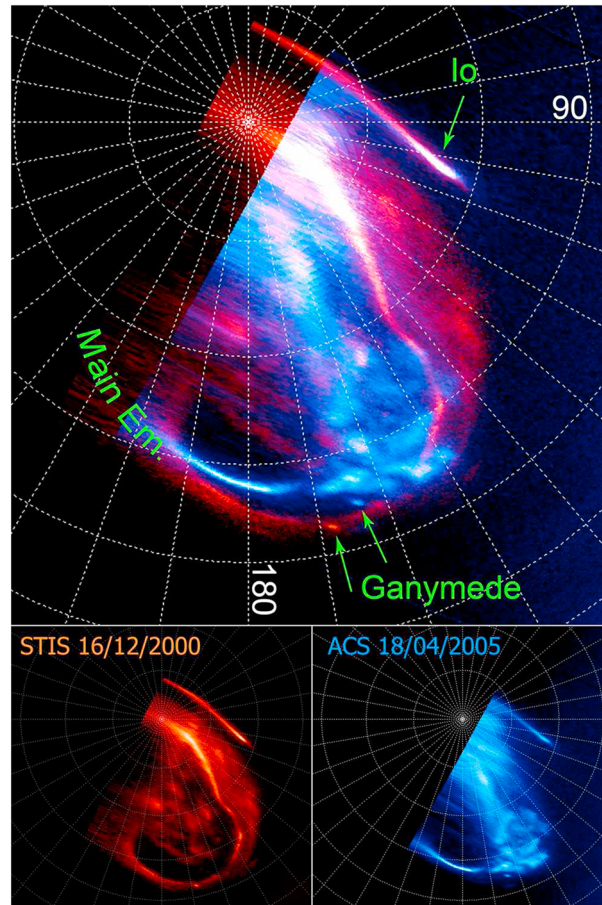


Figure 2. (top) Superposition of the polar projection of two images of Jupiter's northern aurora obtained with HST more than four years apart. The red image was obtained with the Space Telescope Imaging Spectrograph in December 2000, and the blue image was obtained with the Advanced Camera for Surveys camera in April 2005. The 90° and 180° system III meridians have been highlighted on a 10° spaced grid. Green arrows point to the footprints of Ganymede and Io, and the main emission has also been marked. (bottom) Individual polar projections using the same longitude system as in the top panel. From *Grodent et al.* [2008].

where $\beta = p/p_B$ is the plasma beta given by the ratio of the plasma pressure p components to the magnetic field pressure $p_B = B^2/2\mu_0$ [e.g., Cowley, 1978]. Where the MFC is violated, the plasma sheet becomes unstable, the field “balloons”, and a plasmoid is released [McNutt et al., 1987; Southwood and Kivelson, 2001; Kivelson and Southwood, 2005]. McNutt et al. [1987] suggested that this process occurs at radial distances as close as Ganymede's orbit, and although Southwood and Kivelson [2001] disagreed that the process could occur at such small radial distances, they suggested that solar wind-induced magnetospheric compressions and subsequent expansions would increase the parallel pressure and cause the release of plasmoids in the outer magnetosphere once the MFC condition is exceeded. Simulations indicate that parallel pressure does indeed increase during adiabatic flux tube expansion [Vogt et al., 2014]. On the basis of the above observations of pressure anisotropy, Kivelson [2015] has recently suggested that the pressure anisotropy observed at Jupiter is a result of the centrifugal outward transport of plasma and could facilitate the small-scale release of plasma (termed “drizzle” by Bagenal [2007]) down the tail, although it is unclear the degree to which this small-scale drizzle contributes to the large-scale dynamics described by, e.g., Krupp et al. [2004] and Louarn et al. [2014].

Given that pressure anisotropy plays a major role in the force balance in Jupiter's magnetosphere and that the radial stretching of the field is an important parameter for the Jovian M-I coupling current system, we describe here an M-I coupling/magnetodisc model in which the azimuthal current that produces the magnetodisc field includes the contribution from hot plasma pressure anisotropy. We show that the degree of anisotropy indeed affects the structure of the magnetodisc, and thus the location and magnitude of the M-I coupling currents, and the inclusion of pressure anisotropy serves to enhance the effects of changing the hot plasma parameters.

Variations of the latter within the range observed by the Voyager spacecraft then produce latitudinal shifts of the peak main oval field-aligned current and the Ganymede footprint comparable to those observed by Grodent *et al.* [2008].

2. Background Theory

2.1. M-I Coupling Current System Model

The model which describes the M-I coupling current system has been discussed at length in various previous papers [see, e.g., Cowley *et al.*, 2002; Nichols and Cowley, 2004; Nichols, 2011], such that here we give a brief overview. We assume axisymmetry and thus employ a flux function $F(\rho, z)$ related to the poloidal magnetic field via

$$\mathbf{B} = \left(\frac{1}{\rho} \right) \nabla F \times \hat{\phi} , \quad (2)$$

where ρ is the perpendicular distance from the magnetic axis, z is the distance along this axis from the magnetic equator, and ϕ is the azimuthal angle. The use of such a flux function, which is related to the vector potential employed in the calculation of the magnetodisc structure in section 2.2, allows mapping between the equator and ionosphere to be easily achieved by writing $F_e = F_i$, where subscript “e” refers to the equator and “i” refers to the ionosphere. This assumption of axisymmetry therefore vastly simplifies the computations required to model the magnetodisc field structure, facilitating efficient examination of the parameter space, albeit with the cost of losing, e.g., local time information. The model employed here, which is bound by a magnetopause located at $80 R_J$ as discussed below, is likely to be most applicable to the noon sector, valid to a lesser extent in the dawn and dusk sectors and least applicable on the nightside. With this in mind, the validity of the assumption of axisymmetry may be judged from Figure 1 of Ray *et al.* [2014], which indicates that the equatorial magnetic field as modeled by Vogt *et al.* [2011] is essentially axisymmetric inside of $\sim 25 R_J$, beyond which profiles of the magnetic field strength in the dawn, noon, and dusk sectors remain broadly similar out to $100 R_J$, but the nightside profile deviates significantly. With an emphasis on the dayside, and particularly the noon sector, axisymmetry is therefore a reasonable approximation for this model. Further, for our modeling purposes the dipole tilt is not a major issue, since to a first approximation, the plasma will simply subrotate about the instantaneous magnetic axis. The neutral thermosphere will, however, not exactly follow suit, such that future studies in which the axisymmetric assumption is relaxed are clearly warranted. Assuming, then, that the ionospheric magnetic field is a spin-aligned dipole to the lowest approximation, the ionospheric flux function is given by

$$F_i = B_J \rho_i^2 = B_J R_J^2 \sin^2 \theta_i , \quad (3)$$

where B_J is the dipole equatorial magnetic field strength (equal to 426,400 nT in conformity with the VIP4 internal field model of Connerney *et al.* [1998]), R_J is Jupiter’s radius (equal to 71,373 km), ρ_i is the perpendicular distance from the magnetic axis, and θ_i represents magnetic colatitude.

The equation which determines the azimuthal angular velocity ω of plasma steadily diffusing radially outward, termed the “Hill-Pontius” equation, is

$$\frac{\rho_e}{2} \frac{d}{d\rho_e} \left(\frac{\omega}{\Omega_J} \right) + \left(\frac{\omega}{\Omega_J} \right) = \frac{4\pi \Sigma_p^* F_e |B_{ze}|}{\dot{M}} \left(1 - \frac{\omega}{\Omega_J} \right) , \quad (4)$$

where ρ_e is the radial distance at which the field line threads the equatorial plane, Ω_J is the planet’s angular velocity equal to 1.76×10^{-4} rad s^{−1}, and $|B_{ze}|$ is the magnitude of the north-south magnetic field threading the equatorial plane. We employ the “effective” Pedersen conductance Σ_p^* reduced from the true value Σ_p by $\Sigma_p^* = (1 - k_s) \Sigma_p$, where k_s represents the reduction of the angular velocity of the neutral atmosphere (Ω_J^*) from rigid corotation (Ω_J) via “slippage” due to ion-neutral collisions [Huang and Hill, 1989; Millward *et al.*, 2005], such that $(\Omega_J - \Omega_J^*) = k_s(\Omega_J - \omega)$. In common with previous studies we take $k_s = 0.5$, although this is likely an oversimplification [Smith and Aylward, 2009; Tao *et al.*, 2009]. The quantities F_e and $|B_{ze}|$ are given by the magnetodisc model discussed in section 2.2, such that equation (4) is solved numerically (specifically, using `integrate.odeint` in the `scipy` Python package [Jones *et al.*, 2001]) to obtain the equatorial plasma angular velocity.

Considering now the resulting magnetosphere-ionosphere coupling currents, assuming hemispheric symmetry and an ionospheric magnetic field that is vertical and of magnitude $2 B_J$, the total equatorward directed

height- and azimuth-integrated Pedersen current I_p flowing in each ionosphere at the feet of the field lines is given by

$$I_p = 4\pi \Sigma_p^* \Omega_J F_e \left(1 - \frac{\omega}{\Omega_J} \right), \quad (5)$$

which, owing to current continuity, is equal to half the total azimuth-integrated equatorial radial current I_p . The field-aligned current density at the top of the ionosphere $j_{\parallel i}$ is then computed from the divergence of either total field-perpendicular current, such that, in terms of the radial current

$$j_{\parallel i} = \frac{B_J}{2\pi \rho_e |B_{ze}|} \frac{dI_p}{d\rho_e}. \quad (6)$$

2.2. Magnetodisc Model

The magnetodisc model employed is in principle similar to that of N11 and C86, i.e., it is an iterative magnetic potential model. The key differences are that the plasma pressure is in general anisotropic and that the magnetic field vector potential is computed by summing over elliptic integrals rather than employing the analytic scalar potential solution of C86, which explicitly requires pressure isotropy. Otherwise, the plasma input parameters are in most cases identical to those used by N11, taken from Voyager and Galileo observations [Bagenal and Sullivan, 1981; Connerney et al., 1981; Krimigis et al., 1981; McNutt et al., 1981; Siscoe and Summers, 1981; Frank et al., 2002], and any (minor) differences are described below.

The axisymmetric poloidal magnetic field $\mathbf{B}(\rho, z)$ is represented by a vector potential $\mathbf{A}(\rho, z) = A(\rho, z)\hat{\phi}$, related to the magnetic field via $\mathbf{B} = \text{curl}\mathbf{A}$, such that the field components are given by

$$B_\rho = -\frac{\partial A}{\partial z} \quad (7a)$$

and

$$B_z = \frac{1}{\rho} \frac{\partial(\rho A)}{\partial \rho}, \quad (7b)$$

and the flux function F is related via $F = \rho A$, such that a field line is given by $F = \text{constant}$. In general, the magnetic vector potential is related to a current distribution \mathbf{j} through Ampere's law, i.e.,

$$\nabla^2 \mathbf{A} = -\mu_0 \mathbf{j}, \quad (8)$$

where \mathbf{j} is the current density, determined here from the momentum equation for a rotating plasma [e.g., Vasyliūnas, 1983], given by

$$\rho_m \frac{d\mathbf{v}}{dt} = \mathbf{j} \times \mathbf{B} - \text{div} \mathbf{p}, \quad (9)$$

where ρ_m is the plasma mass density, \mathbf{v} is the plasma bulk velocity, and \mathbf{p} is the pressure tensor. Solving for the perpendicular current \mathbf{j}_\perp , assuming a gyrotropic particle distribution function, yields

$$\mathbf{j}_\perp = \frac{\hat{\mathbf{b}}}{B} \times \left[\rho_m \frac{d\mathbf{v}}{dt} + \nabla p_\perp + (p_\parallel - p_\perp)(\hat{\mathbf{b}} \cdot \nabla) \hat{\mathbf{b}} \right], \quad (10)$$

$\hat{\mathbf{b}} = \mathbf{B}/B = (b_\rho, b_z)$ is the unit vector along the magnetic field. The terms in equation (10) represent the plasma inertia, pressure gradient, and pressure anisotropy currents, respectively. The latter term goes to zero when the pressure is isotropic, and the momentum equation then becomes identical to that employed by N11. The anisotropy current $\mathbf{j}_{\perp A}$ can be expressed in terms of the local radius of curvature of the field R given by

$$\frac{1}{R} = |(\hat{\mathbf{b}} \cdot \nabla) \hat{\mathbf{b}}| = \left(\frac{\partial b_\rho}{\partial z} - \frac{\partial b_z}{\partial \rho} \right), \quad (11)$$

such that

$$\mathbf{j}_{\perp A} = \frac{(p_\parallel - p_\perp)}{BR} \hat{\phi}. \quad (12)$$

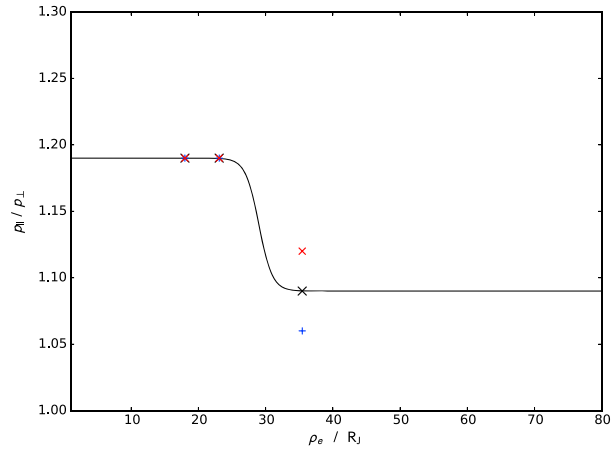


Figure 3. Plot showing the model of the equatorial hot plasma pressure anisotropy ($p_{h||e}/p_{h\perp e}$) versus radial distance ρ_e given by equation (13), based on the measured values of *Paranicas et al.* [1991] shown by the colored symbols. The red crosses, blue pluses, and large black crosses show the values for O^+ , p^+ , and the mean, respectively.

The model is computed on a (ρ, z) grid of resolution $0.1 \times 0.1 R_J$, which is a factor of ~ 4 smaller than the lowest radius of curvature computed in the middle magnetosphere in the results below; hence, the anisotropy current is not limited by the grid resolution.

The plasma is considered to consist of two components, i.e., the hot ~ 30 keV [*Krimigis et al.*, 1981] and cold ~ 100 eV [*McNutt et al.*, 1981; *Frank et al.*, 2002] plasma populations in Jupiter's magnetosphere. The former contributes the majority of the plasma pressure but negligible centrifugal force due to its low density, and vice versa for the latter. Given these relative contributions to the plasma pressure, and the nontrivial variation of the anisotropy of the centrifugally confined cold plasma both along and across the field, we consider here the cold plasma pressure p_c (subscript "c" for cold) to be isotropic, while the hot plasma pressure anisotropy at the equator is given by the *Paranicas et al.* [1991] observations. We thus defer inclusion of cold plasma anisotropy to a later study. Specifically, *Paranicas et al.* [1991] provide six measurements of $(p_{h||e}/p_{h\perp e})$ (subscript "h" for hot), one each for the protons and O^+ ions at radial distances of 18.0, 23.1, and 35.45 R_J on the nightside. While these observations are sparse and limited in local time, these are to our knowledge the only such observations presently available and are thus used here as representative values, and we note that hopefully, Juno will provide further observations of the energetic plasma pressure anisotropy. Specifically, the values for both at the two inner distances are ~ 1.19 , while at 35.45 R_J the values are ~ 1.06 and ~ 1.12 for the protons and O^+ ions, respectively. In the analysis which follows, we consider both the effect of constant values of $(p_{h||e}/p_{h\perp e})$ and a profile based on the measurements described above, i.e.,

$$\left(\frac{p_{h||e}}{p_{h\perp e}} \right) = 1.09 + 0.05 \left[1 - \tanh \left(\frac{\rho_e - 29}{2} \right) \right], \quad (13)$$

which approximates 1.19 inward of 23.1 R_J and the mean value of $(p_{h||e}/p_{h\perp e}) = 1.09$ outward of 35.45 R_J , with a smooth transition between these two values as shown in Figure 3. We then assume for simplicity that the plasma distribution function is bi-Maxwellian such that along a given flux tube the pressures away from the equatorial plane are simply given by

$$p_{h||} = \frac{p_{h||e}}{\left[\frac{p_{h\perp e}}{p_{h||e}} + \frac{B_e}{B} \left(1 - \frac{p_{h\perp e}}{p_{h||e}} \right) \right]} \quad (14a)$$

and

$$p_{h\perp} = \frac{p_{\perp e}}{\left[\frac{p_{h\perp e}}{p_{h||e}} + \frac{B_e}{B} \left(1 - \frac{p_{h\perp e}}{p_{h||e}} \right) \right]^2}. \quad (14b)$$

We set the equatorial values of the perpendicular pressure $p_{h\perp e}$ using the form employed for the (isotropic) hot plasma pressures by C86 and N11, i.e., given by

$$p_{h\perp e}(F) \begin{cases} = \frac{K_h}{V_h(F)} & \text{if } \rho_e \geq 7.5 R_J \\ \propto \rho_e & \text{if } \rho_e < 7.5 R_J \end{cases}, \quad (15)$$

where $V_h(F)$ is the unit flux tube volume for the hot plasma given by

$$V_h = \int \frac{ds}{B} \quad (16)$$

and K_h is a constant. These are in conformity with Voyager and Pioneer observations of the hot plasma outside the Io torus, and C86 showed for Voyager 1 robust values $K_h = 2.5 - 5 \times 10^7 \text{ Pa m T}^{-1}$, while for Voyager 2 and Pioneer data $K_h = 1 - 2 \times 10^7 \text{ Pa m T}^{-1}$. Caudal took $K_h = 3.0 \times 10^7 \text{ Pa m T}^{-1}$ in order to fit the model results to Voyager 1 magnetometer data, although this overestimates the values for Voyager 2 and Pioneer data. Here we employ $K_h = 2.0 \times 10^7 \text{ Pa m T}^{-1}$ as our fiducial value, although we examine the effect of the variation of this parameter over the observed range. We further note that while K_h is a convenient way to specify the equatorial pressure, especially for isotropic pressure, which is constant along field lines, the physical interpretation of $p_{h\perp e} V_h$ is not so straightforward, no longer implying an isothermal medium. However, given the observational data presently available, the use of K_h seems a reasonable initial way to proceed, and no doubt Juno will provide a means of further constraining $p_{h\perp e}$.

The cold plasma pressure, while isotropic, also varies along each field line owing to centrifugal confinement, such that

$$p_c = p_{ce} \exp\left(\frac{\rho^2 - \rho_e^2}{2l^2}\right), \quad (17)$$

where l is the centrifugal equatorial confinement scale height, given for a singly ionized, monoionic plasma with temperature T_c and ion mass m by

$$l = \left(\frac{2k_B T_c}{\omega^2 m}\right)^{\frac{1}{2}}, \quad (18)$$

where k_B is Boltzmann's constant equal to $1.38 \times 10^{-23} \text{ J K}^{-1}$. As previously, we take the ion mass m to be 16 amu. The plasma angular velocity ω is computed by solving the Hill-Pontius equation as described in section 2.1 using the previous iteration of the magnetic field structure. The equatorial values of the cold plasma pressure p_{ce} are, following N11, given by the ideal gas law for a singly ionized plasma

$$p_{ce} = \frac{2N_c k_B T_c}{V_c(F)}, \quad (19)$$

where N_c is the number of cold ions per weber and $V_c(F)$ is the appropriately weighted volume of the unit flux tube given for the centrifugally confined cold plasma by

$$V_c = \int \exp\left(\frac{\rho^2 - \rho_e^2}{2l^2}\right) \frac{ds}{B}. \quad (20)$$

Quantities N_c and T_c are given by profiles derived from Voyager and Galileo data, such that as with N11 we take

$$N_c(\rho_e) = \begin{cases} 0 & \text{if } \rho_e < 5 R_J \\ 10.7 \times 10^{22} & \text{if } 5.7 R_J \leq \rho_e < 7 R_J, \\ 8.1 \times 10^{21} & \text{if } \rho_e \geq 8 R_J \end{cases}, \quad (21)$$

with continuity achieved through linear interpolation between these domains. For the cold plasma temperature, we employ a form that closely approximates the profile given by *Bagenal and Delamere* [2011],

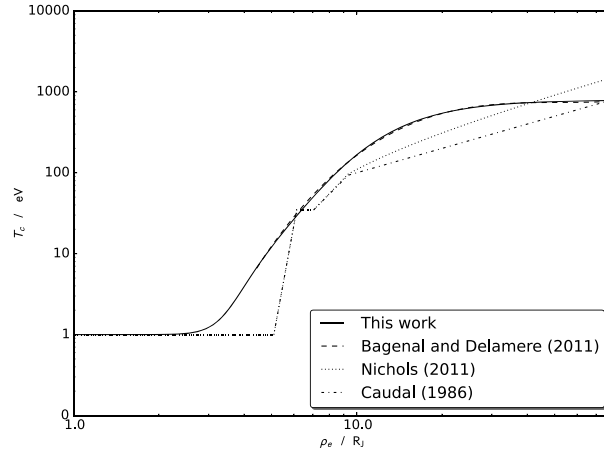


Figure 4. Plot of the cold plasma temperatures in eV given by equation (22) (solid line), along with the profiles of *Bagenal and Delamere* [2011], C86, and N11 as labeled.

Figure 4 beyond $6 R_J$ and asymptotes to 1 eV in the inner region in conformity with the profiles used by C86 and N11, i.e.,

$$\log(k_B T_c(\rho_e)) = \frac{1.45\{1 + \tanh[2.7(\log \rho_e - 0.78)]\}}{1 + \exp\left(\frac{0.55 - \log \rho_e}{0.05}\right)}, \quad (22)$$

which is shown in Figure 4 along with the values used by *Bagenal and Delamere* [2011], N11, and C86 for comparison. Finally, the centrifugal force term in equation (10) is given by

$$j_{\text{cent}} = \frac{p_c \rho}{r^2 B}. \quad (23)$$

Once the azimuthal current distribution \mathbf{j}_\perp has been obtained as described above, the azimuthal vector potential A is computed by summing the contributions ΔA from the current elements ΔI_φ in each model grid cell, given by the classic result for the vector potential of a circular current loop, i.e.,

$$\Delta A = \frac{\mu_0}{\pi} \frac{\Delta I_\varphi a}{\sqrt{a^2 + r_l^2 + 2ar_l \sin \theta_l}} \left[\frac{(2 - k^2)K(k) - 2E(k)}{k^2} \right], \quad (24)$$

where a is the radius of the current loop and (r_l, θ_l) are the radial distance and colatitude with respect to the center and axis of symmetry of the current loop. Quantities $K(k)$ and $E(k)$ are the complete elliptic integrals of the first and second kinds, respectively, given by

$$K(k) = \int_0^{\pi/2} \frac{d\theta}{\sqrt{1 - k^2 \sin^2 \theta}} \quad (25)$$

and

$$E(k) = \int_0^{\pi/2} \sqrt{1 - k^2 \sin^2 \theta} d\theta, \quad (26)$$

and argument k is given by

$$k^2 = \frac{4ar_l \sin \theta_l}{a^2 + r_l^2 + 2ar_l \sin \theta_l}. \quad (27)$$

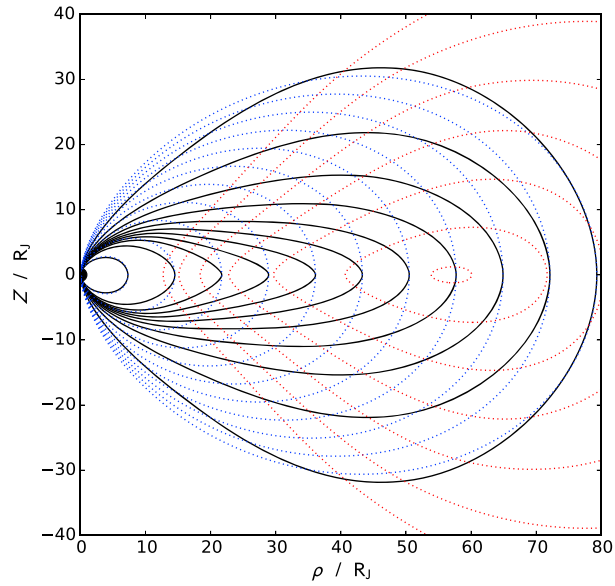


Figure 5. Plot of a representative magnetodisc structure as computed from the present model. The model employs the empirical profile for $(p_{h\parallel e}/p_{h\perp e})$ and $K_h = 5 \times 10^7 \text{ Pa m T}^{-1}$. The solid lines show the overall field lines, while the blue and red dotted lines show the planetary dipole and current sheet field lines, respectively.

Finally, following N11 and C86, at each iteration the vector potential A_s is added to the solution, representing an assumed uniform field of magnitude B_s induced by the equatorial magnetopause current as seen inside the magnetosphere given by

$$A_s = -\frac{B_s \rho}{2} \quad (28)$$

and

$$B_s = 0.6 \frac{2A_{mp}}{R_{mp}}, \quad (29)$$

where R_{mp} is the distance to the equatorial magnetopause, taken to be $80 R_J$, and A_{mp} is the value of A at the equatorial magnetopause. The solution is initiated with the vector potential for a dipole field A_0 given by

$$A_0 = B_J \rho \left(\frac{R_J}{r} \right)^3, \quad (30)$$

where r is radial distance from the center of the planet and proceeds by iteration with the new values of A obtained using the average of A_n and A_{n-1} until convergence. For practicality, we define convergence as occurring when the maximum relative change in A between iterations is $<0.05\%$. A representative-converged magnetic field structure is shown in Figure 5, in which the dotted blue and red lines indicate the planetary dipole and current sheet field lines (i.e., contours of the flux function F), respectively, and the overall magnetodisc structure resulting from the summation of these fields is shown by the black solid lines.

3. Results

3.1. Pressure Anisotropy Ratio

Before examining the model results using the empirical values for the hot plasma pressure anisotropy discussed in section 2.2, we first consider the effects of taking different uniform equatorial values of $(p_{h\parallel e}/p_{h\perp e})$ (which are then mapped toward isotropy along field lines). Figure 6 shows the azimuthal current densities in pA m^{-2} (positive eastward) computed taking $(p_{h\parallel e}/p_{h\perp e}) =$ (a) 0.85, (b) 1.0, and (c) 1.15, i.e., modest pancake, isotropic, and cigar distributions, respectively, with deviations from unity of comparable magnitude to those observed at Jupiter. In each panel, field lines are also shown by the gray contours. It is first apparent from all three cases that, as noted previously by C86 and N11, the hot plasma pressure overall contributes the dominant component of the azimuthal current density with less significant centrifugal and cold plasma

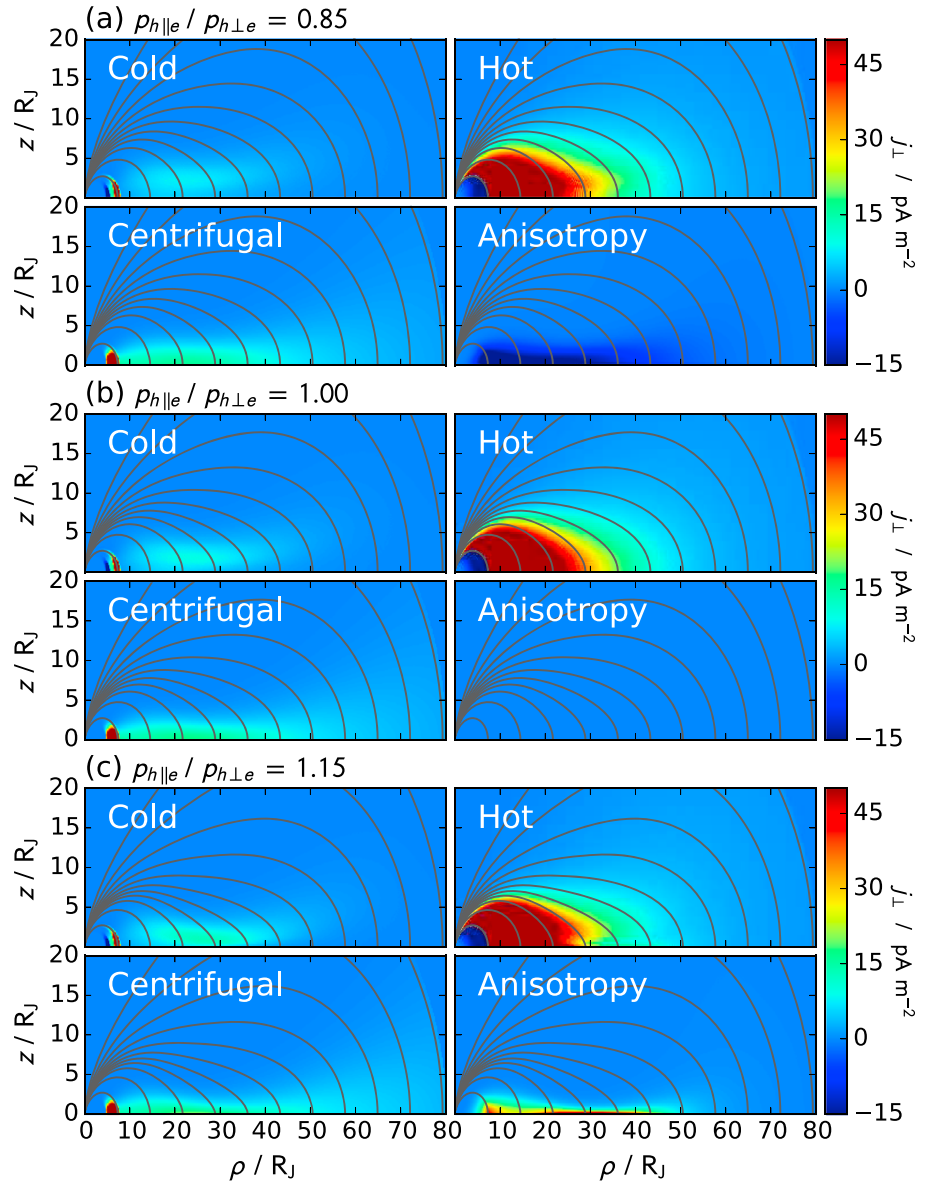


Figure 6. Plots showing the magnetic field lines (gray lines) and azimuthal current contribution (colors) as labeled. Results are shown for constant equatorial value of (a) $(p_{h||e}/p_{h\perp e})=0.85$, (b) $(p_{h||e}/p_{h\perp e})=1.0$, and (c) $(p_{h||e}/p_{h\perp e})=1.15$.

components. The principal result of this work, however, is the inclusion of the anisotropic current density shown in the bottom right of each panel. For $(p_{h||e}/p_{h\perp e})=0.85$, the sense of the anisotropy current is westward, such that the overall azimuthal current density, and thus the degree of radial stretching of the field, is less than for the case with isotropic pressure shown in Figure 6b, which of course has zero anisotropy current. The case with $(p_{h||e}/p_{h\perp e})=1.15$ is most appropriate for the Jovian magnetosphere, given the observations described in section 2. It is apparent that in this case, the majority of the anisotropy current is confined to within $\sim 1.5R_J$ of the equatorial plane, although even with the modest departures from isotropy considered here, the hot plasma pressure anisotropy current reaches values that are comparable to or greater than that of the hot plasma pressure. In the equatorial middle magnetosphere in particular, the anisotropy current provides locally the dominant contribution to the azimuthal current. A secondary effect of the anisotropy current is that the increased stretching of the field acts to modestly increase overall the other current components, further augmenting the field stretching and leading eventually to the firehose instability discussed above. The hot plasma pressure gradient current is further modified from the isotropic case by the variation of $p_{h\perp}$ with distance along the field line away from the equatorial plane. For example, the hot plasma

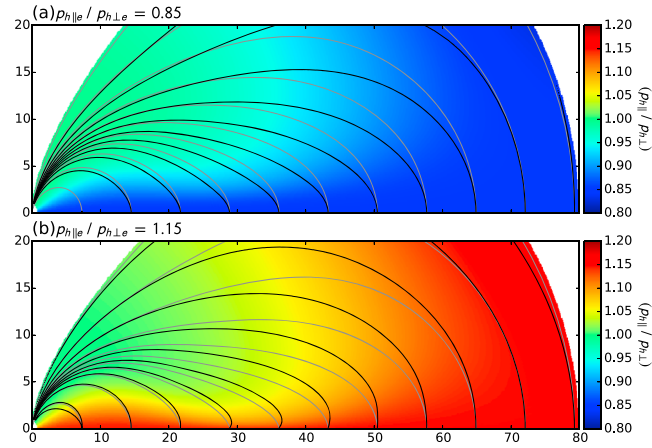


Figure 7. Plots showing the magnetic field lines (gray contours), $p_{h\perp}$ (black contours), and $(p_{h\parallel}/p_{h\perp})$ (colors). Results are shown for constant equatorial value of (a) $(p_{h\parallel}/p_{h\perp})=0.85$ and (b) $(p_{h\parallel}/p_{h\perp})=1.15$.

pressure gradient current is reduced in the region near $z = 1-2R_J$ in the middle magnetosphere for $(p_{h\parallel}/p_{h\perp}) = 1.15$. The reason for this behavior is apparent from the examination of the hot plasma pressure shown in Figure 7. For an isotropic particle distribution function, it follows from Liouville's theorem that the hot plasma pressure is constant along a field line. Anisotropic distributions will, however, tend to isotropize as the magnetic field strength increases away from the equatorial plane, with, e.g., $p_{h\perp}$ increasing for distributions with $(p_{h\parallel}/p_{h\perp}) > 1$ and decreasing for $(p_{h\parallel}/p_{h\perp}) < 1$. Thus, as shown by the colors in Figure 7, in both cases $(p_{h\parallel}/p_{h\perp})$ tends toward 1 with distance along a field line away from the equatorial plane. Contours of $p_{h\perp}$, which over most of the magnetosphere decreases with radial distance, are shown by the black lines. For the isotropic case (not shown), these lines are coincident with the field line contours shown in gray, but for $(p_{h\parallel}/p_{h\perp}) < 1$ it is apparent that $p_{h\perp}$ decreases along the field line with distance away from the equatorial plane, i.e., from the equatorial plane the black contours of $p_{h\perp}$ deflect radially inward from gray field lines. Conversely, for $(p_{h\parallel}/p_{h\perp}) > 1$, $p_{h\perp}$ increases with distance along the field line with distance away from the equatorial plane, i.e., the black contours of $p_{h\perp}$ deflect radially outward from gray field lines. The result of the latter is that, considering the Northern Hemisphere (the Southern Hemisphere is simply the mirror image), $\partial p_{h\perp}/\partial z$ is positive in the near-equatorial middle magnetosphere, where the field strength increases rapidly away from the equatorial plane, and negative at higher latitudes. Thus, the hot plasma pressure gradient current component, given from equation (10) by

$$\mathbf{j}_{\perp h} = \frac{1}{B} \left[b_z \frac{\partial p_{h\perp}}{\partial \rho} - b_\rho \frac{\partial p_{h\perp}}{\partial z} \right] \hat{\phi}, \quad (31)$$

is then reduced in the near-equatorial middle magnetosphere, since b_ρ is positive everywhere. Such effects are minor, however, and the overall effect of pressure anisotropy with $(p_{h\parallel}/p_{h\perp}) > 1$ is to increase the total azimuthal current.

The effects of $(p_{h\parallel}/p_{h\perp})$ are examined further in Figure 8, in which radial profiles of a number of model outputs are shown for $(p_{h\parallel}/p_{h\perp}) = 0.85, 1.0$, and 1.15 using black, blue, and red lines, respectively. Specifically, Figure 8a shows the magnitude of the north-south magnetic field threading the equatorial plane $|B_{ze}|$ in nT computed from equation (7b), Figure 8b the plasma angular velocity normalized to the planet's rotation rate (ω/Ω_J) computed from equation (4), Figure 8c the cold plasma number densities n_c in cm^{-3} calculated from N_c/V_c , Figure 8d the equatorial hot perpendicular and cold plasma pressures in Pa given by equations (15) and (17), Figure 8e the plasma β for the hot perpendicular pressure, cold plasma pressure, and the "plasma β for bulk rotation" (discussed further below), Figure 8f the quantity $\beta_{h\parallel} - \beta_{h\perp}$ related to the MFC discussed above, Figure 8g the magnitude of the equatorial values of the components of the azimuthal current density $j_{\perp e}$ in pA m^{-2} given by each of the terms on the right-hand side of equation (10), and finally Figure 8h the field-aligned current at the top of the ionosphere at the feet of the field lines $j_{\parallel i}$ in $\mu\text{A m}^{-2}$, all plotted versus equatorial radial distance ρ_e in R_J .

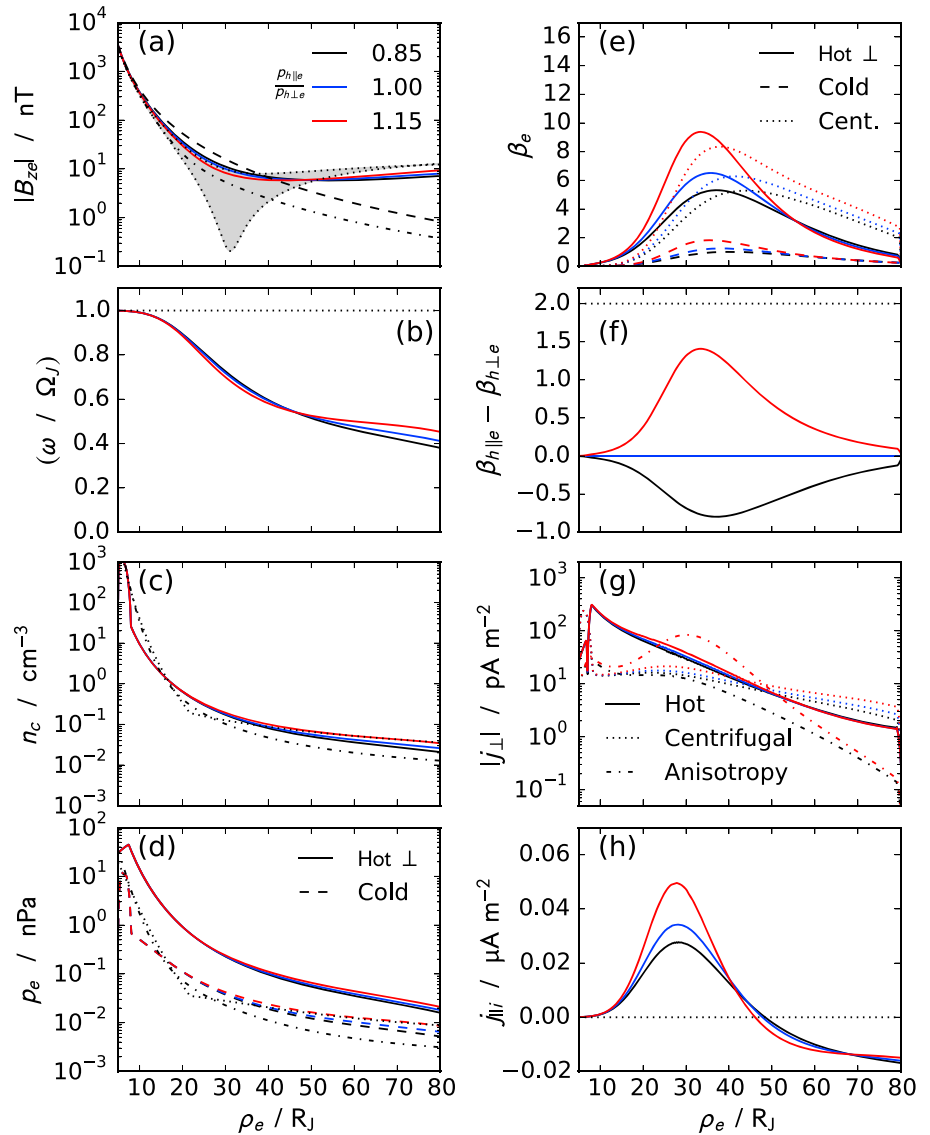


Figure 8. Plots of radial profiles of selected model outputs, shown for $(p_{||e}/p_{\perp e}) = 0.85, 1.0$, and 1.15 using black, blue, and red lines, respectively. Specifically, we show (a) the magnitude of the north-south magnetic field threading the equatorial plane $|B_{ze}|$ in nT computed from equation (7a) along with the dipole (black dashed line), CAN-KK (black dash-dotted line), and dayside Galileo profiles (gray region bounded by the dotted lines); (b) the plasma angular velocity normalized to the planet's rotation rate (ω/Ω_J) computed from equation (4); (c) the cold plasma number density n_c in cm^{-3} calculated from N_c/V_c , along with the profiles of *Frank et al.* [2002] (black dotted line) and *Bagenal and Delamere* [2011] (black dash-dotted line); (d) the equatorial hot perpendicular (colored solid lines) and cold (colored dashed lines) plasma pressures in Pa given by equations (15) and (17), along with pressures computed from *Frank et al.* [2002] and *Bagenal and Delamere* [2011] as discussed in the text; (e) the plasma β for the hot perpendicular pressure, cold plasma, and centrifugal force of bulk rotation as labeled; (f) $\beta_{||e} - \beta_{\perp e}$; (g) the magnitude of the equatorial values of the components of the azimuthal current density $j_{\perp e}$ in pA m^{-2} given by each of the terms on the right-hand side of equation (10) as labeled; and (h) the field-aligned current at the top of the ionosphere at the feet of the corresponding field lines $j_{||}$ in $\mu\text{A m}^{-2}$, all plotted versus equatorial radial distance ρ_e in R_J . The horizontal dotted lines in Figures 8b, 8f, and 8h indicate values of 1, 2, and 0, respectively.

Beginning with the equatorial magnetic field strength in Figure 8a, it is first apparent that the stretching of the field results in the magnitude of the equatorial field decreasing faster than that for a pure dipole in the inner region shown by the dashed line. Figure 8a also shows by the dash-dotted line the *Nichols and Cowley* [2004] approximation to the “CAN” Pioneer/Voyager 1 field model of *Connerney et al.* [1981] and the “KK” Voyager 1 outbound field model of *Khurana and Kivelson* [1993]. Also shown by the gray region bounded by the dotted

lines is the statistical envelope of the dayside Galileo equatorial magnetic field strengths. Specifically, the dotted lines, which are given by

$$|B_{ze}| = B_J \left(\frac{\rho_e}{R_J} \right)^{-3} + a_1 \left(\frac{\rho_e}{R_J} \right)^{a_2} + a_3 \text{ nT}, \quad (32)$$

show polynomial fits to the mean ± 1 standard deviation of the dayside (9–15 h) Galileo equatorial magnetic field strengths. The polynomial coefficients are $a_1 = -1490.53$, $a_2 = -1.19650$, and $a_3 = 19.3758$ (to six significant figures) for the upper bound and $a_1 = -1291.34$, $a_2 = -0.99133$, and $a_3 = 28.8106$ for the lower bound (kindly provided by M. F. Vogt (personal communication, 2014)). As shown previously by N11, the effect of the current sheet field in this axisymmetric model is to reduce the overall field strength inward of $\sim 40 R_J$ and steadily increase the field in the region beyond, these model values being broadly consistent with the upper region of the Galileo envelope over the entire radial range of the model. In the model results the departures from the dipole are amplified and are thus more consistent with the CAN-KK and Galileo values, by increased values of $(p_{h\parallel e}/p_{h\perp e})$, and the $(p_{h\parallel e}/p_{h\perp e}) = 1.15$ profile is consistent with the CAN-KK values out to $\sim 30 R_J$. However, as C86 and N11 discussed, even without the inclusion of anisotropic plasma pressure, if the outward force is sufficiently high, the model does not converge and instead leads to the formation of a neutral point. We were unable to produce converged solutions with magnetic field strengths consistent with the very small values of the lower Galileo envelope in the region near $\sim 30 R_J$, which we suggest indicates that the middle magnetosphere region is inherently unstable or at least approaches that condition for equatorial field strengths comparable to the Galileo “lower envelope”. Turning to the equatorial plasma angular velocity (ω/Ω_J) shown in Figure 8b, it is apparent that increased $(p_{h\parallel e}/p_{h\perp e})$ leads to modestly decreased angular velocities in the inner region, and enhanced values further out, although the changes are small. This results from the relative values of the magnetic field strength shown in Figure 8a for the different values of $(p_{h\parallel e}/p_{h\perp e})$, although all three profiles are consistent with the Kane *et al.* [1995] observation of $(\omega/\Omega_J) \simeq 0.5$ out to $\sim 60 R_J$ and, broadly, those of Krupp *et al.* [2001]. Plasma velocities reported by the latter authors exhibit significant local time variations, which are not captured in our axisymmetric model, with the dawnside magnetosphere roughly corotating out to $\sim 50 R_J$ and the plasma velocities only dropping below $\sim 20\%$ of rigid corotation beyond $80\text{--}100 R_J$ in the midnight and predawn sectors and beyond $50\text{--}60 R_J$ in the premidnight sector. Our model result of $\sim 50\%$ of rigid corotation out to $60 R_J$ is broadly consistent with this range of observations.

The equatorial cold plasma number density n_c and pressure p_e shown in Figures 8c and 8d are compared with Frank *et al.* [2002] (dotted lines) and Bagenal and Delamere [2011] (dash-dotted) polynomial fits to spacecraft data. Note that we have computed the spacecraft plasma pressure from the number densities assuming a singly ionized plasma as for equation (19). It is apparent that over the majority of the magnetosphere the cold ion densities and plasma pressures are broadly in agreement with these profiles, particularly so in the case of Frank *et al.* [2002] profiles and the model results with $(p_{h\parallel e}/p_{h\perp e}) > 1$. As expected, the hot plasma pressure dominates everywhere. Considering now the plasma β given by the ratio of the plasma pressure to the magnetic pressure, we show in Figure 8e the profiles for the hot perpendicular plasma pressure $\beta_{h\perp e}$ and cold plasma pressure β_{ce} , along with the “plasma beta for bulk rotation” $\beta_{cent} = \beta_c \rho^2 / 2l^2$ discussed by, e.g., N11, Achilleos *et al.* [2010], and McNutt [1984]. The plasma β for the parallel component of the hot plasma pressure $\beta_{h\parallel e}$ is given by $\beta_{h\perp e}$ plus the values shown in Figure 8f. As for the model of N11, the hot plasma β dominates inward of $\sim 40 R_J$, outside of which β_{cent} becomes the largest component. This is opposite to the results obtained using C86’s model, for which β_{cent} peaks strongly at ~ 16 near to $\sim 25 R_J$, in contradiction with observed values of ~ 3 at that distance [McNutt, 1984]. N11 obtained values of $\beta_{cent} = 0.75$, 6.63 , and 24.96 at $25 R_J$ for model runs employing $(\Sigma_p^*/\dot{M}) = 10^{-5}$, 10^{-4} , and $5 \times 10^{-4} \text{ mho s kg}^{-1}$, respectively, such that, although he found that the $5 \times 10^{-4} \text{ mho s kg}^{-1}$ magnetic field profile fitted the observed values best, the corresponding β_{cent} significantly overestimated the observed values in the middle magnetosphere. Our values of ~ 2.0 , 2.5 , and 3.6 at $25 R_J$ for $(p_{h\parallel e}/p_{h\perp e}) = 0.85$, 1.0 , and 1.15 , respectively, are in much better agreement with the observed values than that for the model of N11. A further implication of the inclusion of anisotropic pressure concerns the stability of the magnetosphere, as discussed in section 1. The dotted line in Figure 8f indicates the MFC given by equation (1), i.e., if the quantity $\beta_{h\parallel e} - \beta_{h\perp e} > 2$, the system is in violation of the firehose stability condition, and the field will undergo “ballooning”; indeed, our model does not converge once $\beta_{h\parallel e} - \beta_{h\perp e} > 2$. It is apparent that for our fiducial model, even with the modest cigar anisotropy of $(p_{h\parallel e}/p_{h\perp e}) = 1.15$, the conditions are marginally stable in the middle magnetosphere, with $\beta_{h\parallel e} - \beta_{h\perp e}$ peaking at ~ 1.5 near $\sim 30 R_J$,

and a number of modest changes to parameter values within the observed ranges (e.g., Σ_p^* or K_h) produce runs that violate the MFC. We discuss the implications of this in section 4.

Considering now the magnitude of the equatorial azimuthal current shown in Figure 8g, we show the contributions from the hot plasma pressure gradient, centrifugal force, and pressure anisotropy using the solid, dotted, and dash-dotted lines, respectively. For the latter, we note that the sense of the current is eastward for $(p_{h\parallel e}/p_{h\perp e}) > 1$, and vice versa, such that the black dash-dotted line corresponds to algebraically negative current density. We first confirm the conclusion of N11 that it is the centrifugal force term that dominates in the outer magnetosphere beyond $\sim 45\text{--}50 R_J$, and for $(p_{h\parallel e}/p_{h\perp e}) \leq 1$ the hot plasma provides the dominant contribution inward of this distance. This is also in broad conformity with *Achilleos et al.*'s [2010] discussion of a "transition distance," beyond which the rotational kinetic energy of the plasma exceeds its thermal energy given by

$$\rho_T^2 = 2mI^2 \left(\frac{\beta_{h\perp e}}{\beta_{ce}} \right), \quad (33)$$

where m is the magnitude of the exponent of the radial dependence of the equatorial field strength (given, e.g., for a dipole field by $m = 3$). It is worth noting that, using $m = 3$, the distances at which ρ_e becomes larger than ρ_T are $\sim 55\text{--}70 R_J$ in the present model, although it is clear that field strength does not follow a power law, and indeed, the weak dependence of the field strength on radial distance in the middle magnetosphere is consistent with lower values of ρ_T than for the dipole. By comparison with our model results, then, the transition distance of *Achilleos et al.* [2010] provides a reasonable estimation of where the rotational kinetic energy becomes dominant. However, the principal result is that for $(p_{h\parallel e}/p_{h\perp e}) > 1$ the pressure anisotropy term dominates in the middle magnetosphere, where the field is most radially stretched, and our fiducial model provides the largest contribution to the azimuthal current between ~ 24 and $48 R_J$, before dropping off to negligible values in the outer magnetosphere. For $(p_{h\parallel e}/p_{h\perp e}) = 1$ the anisotropy current is absent, while for $(p_{h\parallel e}/p_{h\perp e}) < 1$ the westward current acts to dipolarize the field and thus produces low values of current owing to the increased radius of curvature of the field.

Turning finally to the field-aligned component of the magnetosphere-ionosphere coupling currents shown in Figure 8h, as discussed previously by N11, the radial distension of the field acts to modify the location and magnitude of the peak upward field-aligned current. The field-aligned current profile for $(p_{h\parallel e}/p_{h\perp e}) = 0.85$ differs only slightly from that for isotropic pressure, with the upward current peaking at $\sim 0.028 \mu\text{A m}^{-2}$ at $\sim 28.3 R_J$ for the former case and at $0.034 \mu\text{A m}^{-2}$ at $\sim 28.0 R_J$ for the latter. However, it is evident that the field-aligned current profile for $(p_{h\parallel e}/p_{h\perp e}) = 1.15$ differs more substantially, with a peak of $0.050 \mu\text{A m}^{-2}$ at $\sim 27.8 R_J$. In all cases, the field-aligned current density is negative in the outer magnetosphere beyond $\sim 45\text{--}50 R_J$, resulting from the increasing equatorial field strength in this region owing to the current sheet field, which as was suggested by N11 possibly corresponds to the dark polar region observed immediately poleward of the main oval, particularly on the dawnside but sometimes at all local times [*Grodent et al.*, 2003b; *Nichols et al.*, 2009].

The effect of varying $(p_{h\parallel e}/p_{h\perp e})$ on the location and magnitude of the magnetosphere-ionosphere coupling currents is considered further in Figure 9, in which we show the peak total equatorial radial current $I_{p\max}$ in MA, (b) the peak field-aligned current density at the top of the ionosphere $j_{\parallel i\max}$ in $\mu\text{A m}^{-2}$, (c) the equatorial radial distance of the peak field-aligned current $\rho_{ej_{\parallel i\max}}$ in R_J , and (d) the ionospheric colatitude θ_i of the peak field-aligned current (pluses) and the mapped ionospheric location of the equatorial radial distance of Ganymede's orbit, thus representing the Ganymede footprint (crosses), all versus $(p_{h\parallel e}/p_{h\perp e})$. Overall, the effect of increased $(p_{h\parallel e}/p_{h\perp e})$ is to increase the magnitude of the peak currents and, where $(p_{h\parallel e}/p_{h\perp e}) > 1$, to decrease the radial distance of the peak field-aligned current. Specifically, the peak currents $I_{p\max}$ and $j_{\parallel i\max}$ increase from ~ 21 to 26 MA and from ~ 0.028 to $0.050 \mu\text{A m}^{-2}$ as $(p_{h\parallel e}/p_{h\perp e})$ increases from 0.85 to 1.15 , as discussed above, although it is evident that the gradient increases when $(p_{h\parallel e}/p_{h\perp e}) > 1$. The equatorial radial distance of the peak field-aligned current is around $\sim 28 R_J$ for $(p_{h\parallel e}/p_{h\perp e}) \leq 1$ and decreases to $\sim 26.3 R_J$ for $(p_{h\parallel e}/p_{h\perp e}) = 1.15$. Correspondingly, the ionospheric colatitude of the peak field-aligned current increases from $\sim 14.7^\circ$ to $\sim 15.8^\circ$, and the increased radial distension of the field causes the colatitude of the Ganymede footprint to increase modestly from $\sim 17.1^\circ$ to $\sim 17.5^\circ$.

3.2. Hot Plasma Parameter K_h

The above discussion provides an overview of the effect on the magnetodisc and magnetosphere-ionosphere coupling current system of varying the (uniform in the equatorial plane) hot plasma pressure

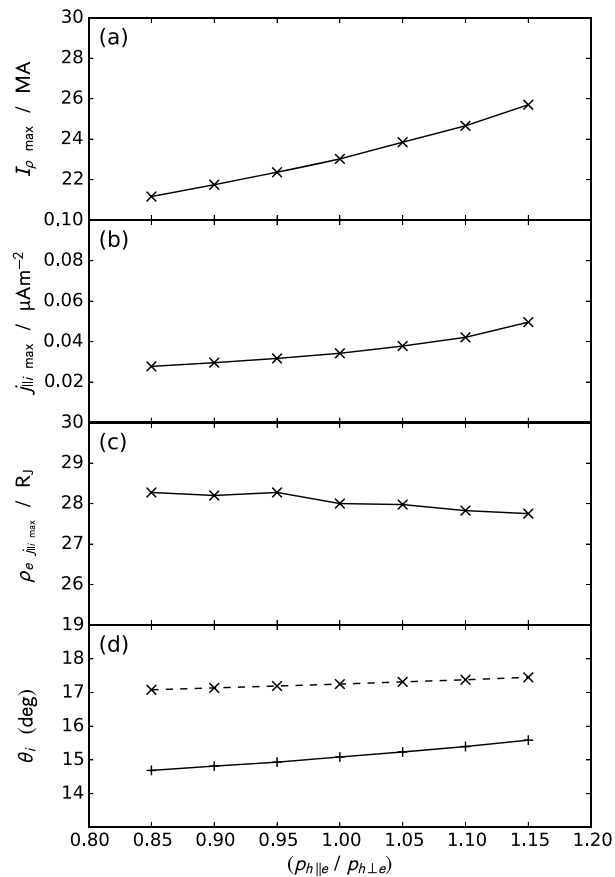


Figure 9. Plot showing (a) the peak total equatorial radial current $I_{\rho \max}$ in MA, (b) the peak field-aligned current density at the top of the ionosphere $j_{||i \max}$ in $\mu\text{A m}^{-2}$, (c) the equatorial radial distance of the peak field-aligned current $\rho_e j_{||i \max}$ in R_J , and (d) the ionospheric colatitude θ_i of the peak field-aligned current (pluses joined by solid lines) and the Ganymede footprint (crosses joined by dashed lines), all versus $(p_{h||e}/p_{h\perp e})$.

anisotropy $(p_{h||e}/p_{h\perp e})$. However, as discussed in section 2, *Paranicas et al.* [1991] provided measurements of the anisotropy of the hot equatorial plasma, which we have modeled using equation (13) as shown in Figure 3. Employing this empirical form for the hot plasma pressure anisotropy and noting the variation in the parameter K_h observed in the Voyager and Pioneer data as discussed above, we now consider the effect of varying K_h around the fiducial value of $K_h = 2.0 \times 10^7 \text{ Pa m T}^{-1}$. We first show in Figure 10 the magnetodisc structures and azimuthal current densities for $K_h =$ (a) 1.5, (b) 2.0, and (c) $2.5 \times 10^7 \text{ Pa m T}^{-1}$, respectively, in the same format as for Figure 6. It is again evident that the hot plasma pressure gradient provides the most significant contribution to the azimuthal current overall but that the hot plasma anisotropy current increases greatly as the value of K_h rises. The increased stretching of the field also results in modest rises in the cold plasma pressure and centrifugal current densities, and with all currents overall confined more closely to the equatorial plane, although the local reduction of the hot plasma pressure gradient current in the near-equatorial middle magnetosphere, as discussed above, is accentuated as the field becomes increasingly stretched with increasing K_h .

The effects of varying K_h on the magnetodisc and magnetosphere-ionosphere coupling current system are examined further in Figure 11 in the same format as Figure 8. Considering first $|B_{ze}|$ shown in Figure 11a, it is apparent that the increasingly stretched magnetic field associated with higher values of K_h leads to lower values of $|B_{ze}|$, with the profile for $K_h = 2.5 \times 10^7 \text{ Pa m T}^{-1}$ tracking the lower boundary of the Galileo envelope out to $\sim 20 R_J$ and the CAN-KK profile out to $\sim 25 R_J$ before diverting toward increasing values consistent with the Galileo profile in the outer magnetosphere. The slight “kink” in the magnetic field that strengths around $\sim 29 R_J$ is a result of the transition in the $(p_{h||e}/p_{h\perp e})$ model values from 1.19 to 1.09 in this region, as shown in Figure 3. A key feature of varying K_h is that it affects the structure of the field as far inward as the Io plasma

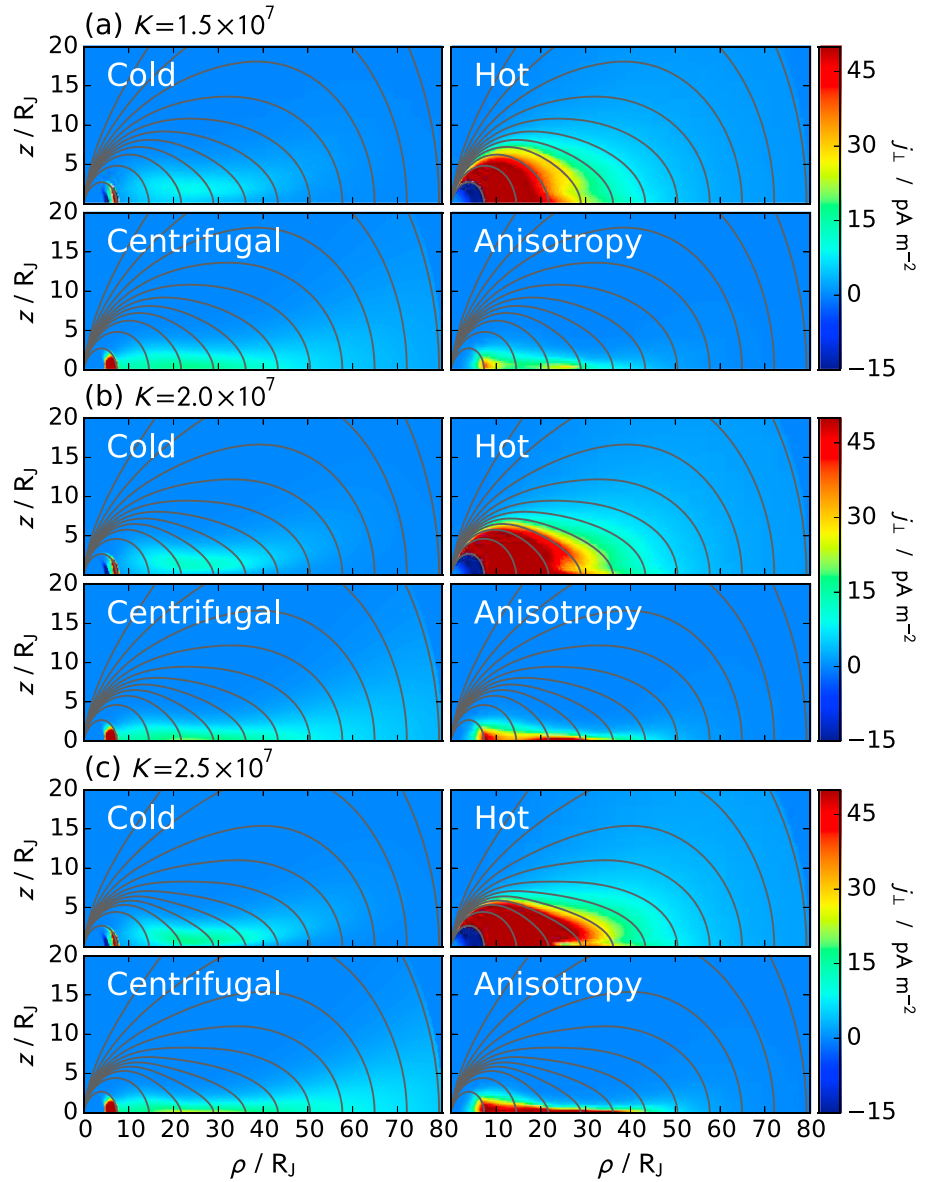


Figure 10. As for Figure 6 but using the empirical model for $(p_{h\parallel e}/p_{h\perp e})$, and $K_h =$ (a) 1.5, (b) 2.0, and (c) 2.5×10^7 Pa m T $^{-1}$, respectively.

torus, since the hot plasma pressure gradient current dominates this far in. This results in significant changes in the mapping between the ionosphere and equator in the inner region, with implications for the ionospheric mapping of the Ganymede footprint and main auroral oval, as discussed below. The angular velocity profiles are broadly similar, following the same pattern as for Figure 8b, i.e., with the angular velocity decreasing faster in the inner region and slower farther out, with (ω/Ω_J) values in the outer magnetosphere of ~ 0.4 – 0.5 . The cold plasma number densities and pressures, shown in Figures 11c and 11d, indicate that the model produces values broadly consistent with the profiles of Frank *et al.* [2002] over the entire radial range of the model, particularly so over distances outward of $\sim 40 R_J$ for the case employing our fiducial value of $K_h = 2.0 \times 10^7$ Pa m T $^{-1}$. It is again apparent that the hot plasma pressure everywhere dominates that of the cold plasma, and this is reflected in the plasma β shown in Figure 11e. As for Figure 8e, the β profiles are such that the hot plasma dominates in the inner region, while the β_{cent} is the largest further out, with the transitions occurring at $\sim 29, 37$, and $41 R_J$ for $K_h = 1.5, 2.0$, and 2.5×10^7 Pa m T $^{-1}$, respectively, i.e., reflecting the increased significance of the hot plasma as K_h increases. The “kinked” or double-peaked nature of the plasma β profiles results from the transition between values of $(p_{h\parallel e}/p_{h\perp e})$ in the model and the values of β_{cent} at $25 R_J$, i.e., $\sim 2.3, \sim 3.2$,

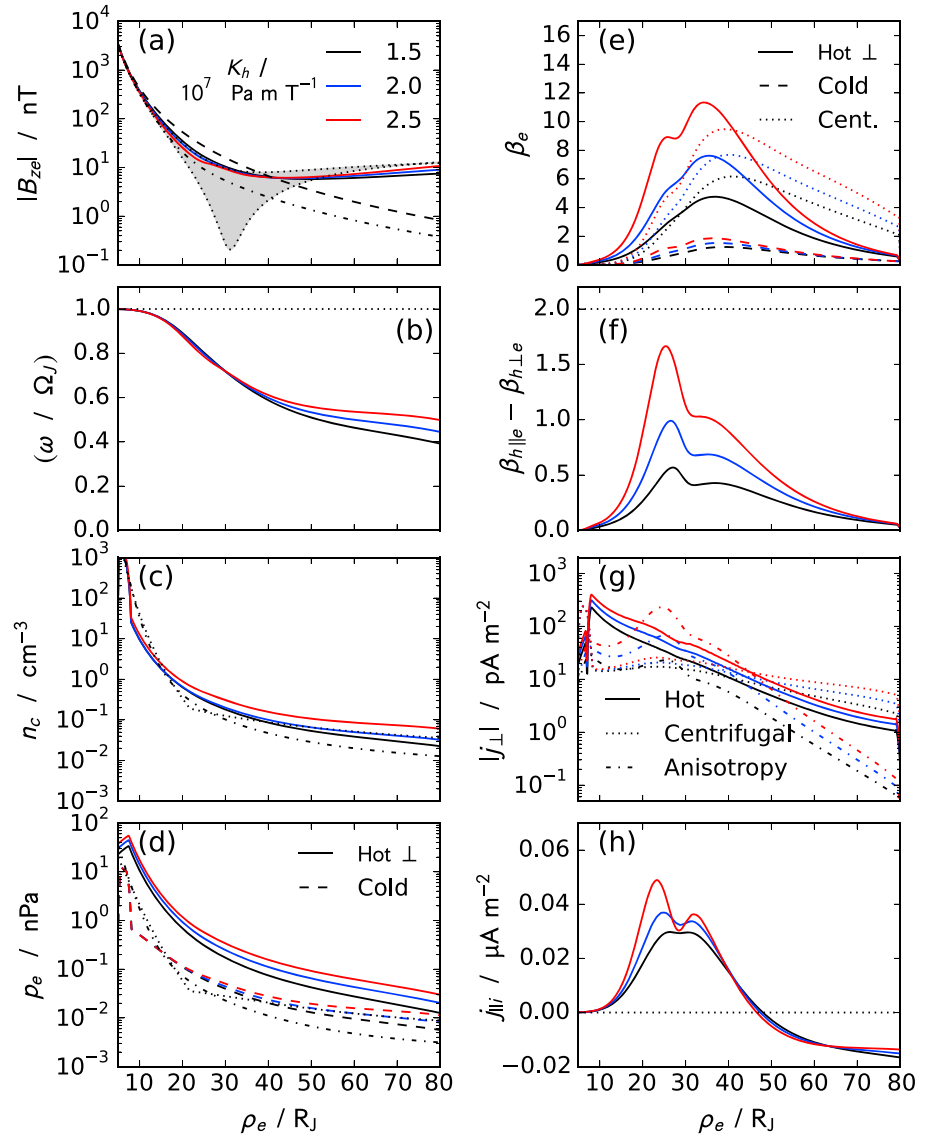


Figure 11. As for Figure 8 but using the empirical model for $(p_{h\parallel e}/p_{h\perp e})$, and $K_h =$ (a) 1.5, (b) 2.0, and (c) $2.5 \times 10^7 \text{ Pa m T}^{-1}$, respectively.

and ~ 4.5 for $K_h = 1.5, 2.0$, and $2.5 \times 10^7 \text{ Pa m T}^{-1}$, respectively, are again largely consistent with the observed value of ~ 3 at this distance, with the fiducial model the closest.

Considering now the susceptibility of the magnetosphere to the firehose instability, we show profiles of $\beta_{h\parallel e} - \beta_{h\perp e}$ in Figure 11f. The values are the largest inward of $\sim 30 R_J$ owing to the form of the $(p_{h\parallel e}/p_{h\perp e})$ model, and the peak value of $\beta_{h\parallel e} - \beta_{h\perp e}$ increases with increasing K_h . With $K_h = 2.5 \times 10^7 \text{ Pa m T}^{-1}$, the peak value of $\beta_{h\parallel e} - \beta_{h\perp e}$ is ~ 1.7 at $\sim 23 R_J$, i.e., it is evident that $K_h = 2.5 \times 10^7 \text{ Pa m T}^{-1}$ produces values that are close to violating the MFC. The peak value of $\beta_{h\parallel e} - \beta_{h\perp e}$ increases quickly with K_h , and tests indicate that this condition is reached with $K_h \simeq 2.6 \times 10^7 \text{ Pa m T}^{-1}$. Thus, at least with the plasma and M-I coupling parameters employed here, larger values of K_h such as those observed during the Voyager 1 pass as discussed above would imply a magnetosphere susceptible to ballooning in the middle magnetosphere region around $\sim 20\text{--}30 R_J$ as discussed by, e.g., *Kivelson and Southwood* [2005]. We discuss this further in section 4. Turning now to the azimuthal currents shown in Figure 11g, as discussed above the hot plasma pressure gradient dominates in the inner region outside the torus, and the centrifugal current is the largest in the outer magnetosphere beyond $\sim 40\text{--}50 R_J$. However, the hot plasma pressure anisotropy current peaks at $\sim 24\text{--}26 R_J$ and is

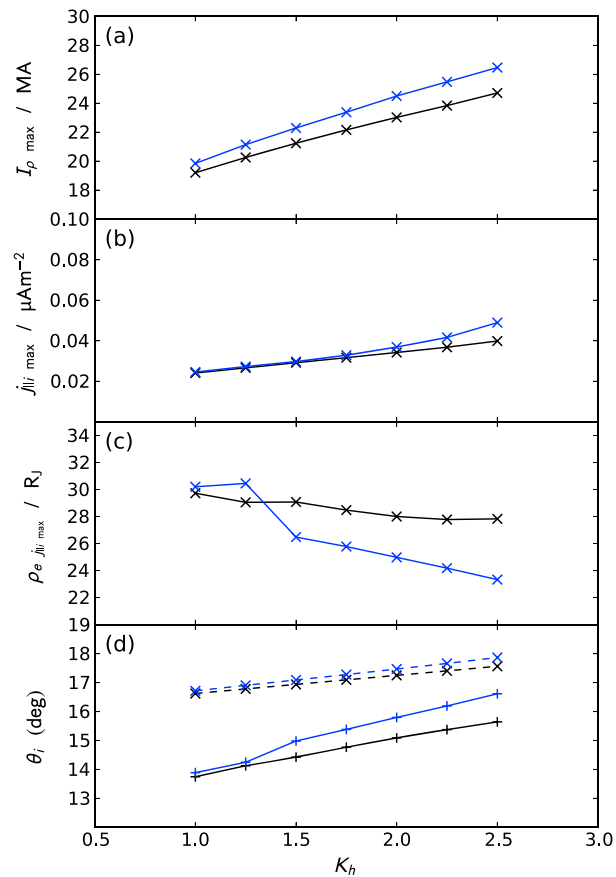


Figure 12. As for Figure 9 but with varying K_h . Black symbols indicate results with isotropic pressure, while blue indicates results using the empirical model for $(p_{h\parallel e}/p_{h\perp e})$.

comparable to or greater than the hot plasma current over $\sim 20\text{--}50 R_J$, thus providing a significant contribution to the force balance in the middle magnetosphere.

Considering now the field-aligned current at the top of the ionosphere shown in Figure 11h, it can be seen that increasing K_h increases the peak field-aligned current density and shifts it inward with peaks at ~ 0.03 , 0.04 , and 0.05 at ~ 26 , 25 , and $23 R_J$ for $K_h = 1.5$, 2.0 , and $2.5 \times 10^7 \text{ Pa m T}^{-1}$, respectively. It is evident that the field-aligned current profile is substantially affected by the change in anisotropy values in the middle magnetosphere, resulting in the appearance of a two-peak structure for higher values of K_h . This results in an equatorward shift of the ionospheric mapping of the peak field-aligned current in addition to that owing to the increasingly stretched field discussed further below. For $K_h = 2.5 \times 10^7 \text{ Pa m T}^{-1}$, the two peaks map to $\sim 16.1^\circ$ and $\sim 16.9^\circ$ within an overall feature of width $\sim 2^\circ$, such that this would be a minor effect. No such small-scale feature has been reported in HST images of the auroras, but the high signal-to-noise of forthcoming Juno UVS observations may reveal such forms, as the Cassini UVIS instrument has at Saturn. The field-aligned current density is again negative in the region beyond $\sim 46\text{--}48 R_J$.

We finally consider the effect of changing K_h on the magnetosphere-ionosphere coupling currents, as shown in Figure 12 in the same format as for Figure 9, except that the black symbols indicate results with isotropic hot plasma pressure, while blue symbols indicate values obtained employing the anisotropic pressure model. In both cases, increased K_h results in increased peak current magnitudes as shown in Figures 12a and 12b, with I_{ρ} and j_{\parallel} increasing faster with anisotropic pressure, particularly so for j_{\parallel} when $K_h > 2.0 \times 10^7 \text{ Pa m T}^{-1}$ owing to the additional radial stretching of the field due to the anisotropy current. As previously indicated in Figure 11h, the radial distance of the peak field-aligned current shown in Figure 12c decreases with increasing K_h , modestly so for the case with isotropic pressure and more significantly with anisotropic pressure. The effects of the appearance of the two-peak current profile are also evident by the large inward shift of the peak from ~ 30 to $26 R_J$ over the range $K_h > 1.25\text{--}1.5 \times 10^7 \text{ Pa m T}^{-1}$. Finally, the ionospheric colatitude

of the peak field-aligned current (pluses) and the Ganymede footprint (crosses) are shown in Figure 12d. Between $K_h > 1.0 - 2.5 \times 10^7 \text{ Pa m T}^{-1}$ the ionospheric colatitude of the peak field-aligned current increases from $\sim 13.7^\circ$ (13.9°) to $\sim 15.6^\circ$ (16.6°), while over the same range the Ganymede footprint latitude increases from $\sim 16.6^\circ$ (16.7°) to $\sim 17.6^\circ$ (17.9°) for isotropic (anisotropic) hot plasma pressure. It is thus evident that while isotropic pressure variations in the hot plasma parameter K_h within the observed range produce significant changes in the ionospheric colatitudes of these features, including the effects of anisotropic pressure increases these shifts by $\sim 20 - 45\%$. Significantly, with anisotropic pressure, the variations of $\sim 2.7^\circ$ and $\sim 1.2^\circ$ for the peak field-aligned current and Ganymede footprints over the range $K_h > 1.0 - 2.5 \times 10^7 \text{ Pa m T}^{-1}$ are comparable to the shifts observed by *Grodent et al.* [2008].

4. Discussion

We first note that our fiducial model produces results broadly consistent with the Galileo profiles of the magnetic field and plasma parameters over the whole radial range of the model. Second, although the hot plasma pressure anisotropies measured by *Paranicas et al.* [1991] are relatively modest, it is evident that hot plasma pressure anisotropy provides a significant, if not dominant, contribution to the force balance in Jupiter's middle magnetosphere, particularly over equatorial radial distances of $\sim 20 - 50 R_J$. Inward of this location, the hot plasma pressure gradient is dominant, and outward the centrifugal force is the largest. Inclusion of the anisotropy current enhances the effects of variation of the hot plasma parameter $K_h = p_h V_h$. This parameter is of particular relevance for the observed variation in the latitude of the Ganymede footprint, since the hot plasma pressure gradient term is the largest at $15 R_J$, typically followed by the anisotropy current. Although the observed values of K_h are $1 - 5 \times 10^7 \text{ Pa m T}^{-1}$, we have produced results with $K_h \leq 2.5 \times 10^7 \text{ Pa m T}^{-1}$, since above this value the MFC is violated in the middle magnetosphere near $\sim 25 R_J$, and the model does not converge. For $K_h = 2.0 - 2.5 \times 10^7 \text{ Pa m T}^{-1}$ the peak value of $\beta_{h\parallel e} - \beta_{h\perp e}$ is $\sim 1 - 2$, implying that Jupiter's magnetosphere is typically marginally stable or actually unstable in the middle magnetosphere. We should qualify this statement by recalling that we have not considered here the contribution of the cold plasma pressure anisotropy, which may also be of significant importance, and we will address this in future works. However, from these results, we may expect to observe small-scale plasmoids or drizzle originating in the middle magnetosphere, i.e., not as far as in Ganymede but surprisingly close in nonetheless. These would be observable in situ by Juno during the early-mid phases of the mission as the spacecraft enters the current sheet region around $\sim 25 R_J$, and the significant decrease in the lower bound of the statistical envelope of magnetic field strengths around $\sim 30 R_J$ observed in the Galileo data may be a signature of this instability. Such initially small-scale forms may then be related to the "magnetic nulls" observed in the outer magnetosphere as the plasma mass is transported outward. We further conjecture that a process which acts to increase the parallel pressure still further, such as the rotation of a flux tube through the dusk sector or an expansion following a previous compression as discussed by *Southwood and Kivelson* [2001] and *Kivelson and Southwood* [2005], may induce increased mass loss and plasmoid formation throughout the dayside/dusk magnetosphere. This process may explain the arcs and generally disturbed auroral morphology poleward of the main oval in the few days following the onset of a compression [*Nichols et al.*, 2009]. We note that a similar conjecture has also been recently put forward by *Delamere et al.* [2015]. Examination of the effects of compressions and expansions will be conducted in future works. Further, it is worth noting that *Mauk et al.* [1999] discussed "storm-like" interchange events in the middle magnetosphere, which may well be associated with susceptibility to the firehose instability in this region.

Regarding the latitudinal shifts of the main oval and the Ganymede footprint, it is apparent that with the inclusion of anisotropic hot plasma pressure, the variation of the hot plasma parameter K_h is a possible candidate to explain the shifts observed by *Grodent et al.* [2008]. In this case, the poleward (blue) shifted auroras in Figure 2 would correspond to low values of K_h , while the equatorward (orange) case would imply higher values of K_h . The situation is probably not this simple, as, e.g., the main emission appears brighter for the case with the poleward shift, which is opposite to what might be expected on the basis of these results, although it must be noted that there are a number of other factors, such as the iogenic plasma mass outflow rate and Pedersen conductance, the variation of which may also affect the brightness of the main oval. Further, although the $\sim 1.2^\circ$ shift in the Ganymede footprint is the largest computed while remaining within observed parameter ranges, it is still slightly smaller than the $\sim 2^\circ$ observed by *Grodent et al.* [2008], also indicating compounding effects. Another aspect worth future investigation is the potential link between variability in hot plasma pressure and iogenic plasma mass outflow rate \dot{M} . For example, an episode of enhanced \dot{M}

may plausibly lead to, eventually, a corresponding episode of enhanced plasma energization associated with augmented mass loss via plasmoid production. N11 examined the effects on magnetodisc structure of varying \dot{M} , but a self-consistent investigation incorporating variation of hot plasma pressure is clearly warranted.

5. Summary

We have presented a model of force balance in Jupiter's magnetodisc that includes the effects of hot plasma pressure anisotropy. The magnetic field is computed using an iterative vector potential model, with the current sheet magnetic field computed from the sum of the azimuthal current components arising from the plasma pressure gradient, pressure anisotropy, and centrifugal forces. The fiducial model produces results that are consistent with both magnetic field and plasma data over the whole radial range of the model. The hot plasma pressure gradient and centrifugal forces dominate in the regions inward of $\sim 20 R_J$ and outward of $\sim 50 R_J$, respectively, while for realistic values of the pressure anisotropy, the anisotropy current is either the dominant component or at least comparable with the hot plasma pressure gradient in the region in between. The inclusion of hot plasma pressure anisotropy increases by ~ 20 – 45% the shifts in the latitude of the main oval and Ganymede footprint associated with realistic variations in the hot plasma parameter $K_h = p_h V_h$. Such shifts of $\sim 2.7^\circ$ and $\sim 1.2^\circ$ for the peak field-aligned current and Ganymede footprints, respectively, for $K_h > 1.0$ – $2.5 \times 10^7 \text{ Pa m T}^{-1}$ are comparable to the shifts observed by Grodent *et al.* [2008]. However, the middle magnetosphere is susceptible to the firehose instability, with peak values of $\beta_{h\parallel e} - \beta_{h\perp e}$ of ~ 1 – 2 , for $K_h = 2.0$ – $2.5 \times 10^7 \text{ Pa m T}^{-1}$. Larger values of K_h , still well within the observed range, yield results with $\beta_{h\parallel e} - \beta_{h\perp e} > 2$ near $\sim 25 R_J$, and the model does not converge. This suggests that small-scale plasmoid release or drizzle of iogenic plasma may occur in the middle magnetosphere and that processes that increase the parallel pressure, such as magnetospheric expansions, may intensify this mass loss process. We conjecture that such processes may give rise to the arc forms and disturbed auroral morphologies that occur during the few days following compression region onset.

Acknowledgments

J.D.N. was supported by STFC Advanced Fellowship (ST/I004084/1). S.W.H.C. was supported by STFC Consolidated grant ST/K001000/1. N.A. was supported in part of this work by STFC Consolidated grant (UCL Astrophysics) ST/J001511/1. J.D.N. thanks M.F. Vogt for provision of the Galileo magnetic field profiles. The computational model described in this paper is available upon application to J.D.N.

References

- Achilleos, N., P. Guio, and C. S. Arridge (2010), A model of force balance in Saturn's magnetodisc, *Mon. Not. R. Astron. Soc.*, **401**(4), 2349–2371, doi:10.1111/j.1365-2966.2009.15865.x.
- Bagenal, F. (1994), Empirical model of the Io plasma torus: Voyager measurements, *J. Geophys. Res.*, **99**(A6), 11,043–11,062, doi:10.1029/93JA02908.
- Bagenal, F. (2007), The magnetosphere of Jupiter: Coupling the equator to the poles, *J. Atmos. Sol. Terr. Phys.*, **69**(3), 387–402, doi:10.1016/j.jastp.2006.08.012.
- Bagenal, F., and P. A. Delamere (2011), Flow of mass and energy in the magnetospheres of Jupiter and Saturn, *J. Geophys. Res.*, **116**, A05209, doi:10.1029/2010JA016294.
- Bagenal, F., and J. D. Sullivan (1981), Direct plasma measurements in the Io torus and inner magnetosphere of Jupiter, *J. Geophys. Res.*, **86**(A10), 8447–8466, doi:10.1029/JA086ia10p08447.
- Caudal, G. (1986), A self-consistent model of Jupiter's magnetodisc including the effects of centrifugal force and pressure, *J. Geophys. Res.*, **91**(A4), 4201–4221, doi:10.1029/JA091ia04p04201.
- Clarke, J. T., D. Grodent, S. W. H. Cowley, E. J. Bunce, P. M. Zarka, J. E. P. Connerney, and T. Satoh (2004), Jupiter's aurora, in *Jupiter: The Planet, Satellites and Magnetosphere*, edited by F. Bagenal and W. B. McKinnon, pp. 639–670, Cambridge Univ. Press, Cambridge, U. K.
- Connerney, J. E. P., M. H. Acuña, and N. F. Ness (1981), Modeling the Jovian current sheet and inner magnetosphere, *J. Geophys. Res.*, **86**, 8370–8384.
- Connerney, J. E. P., M. H. Acuña, N. F. Ness, and T. Satoh (1998), New models of Jupiter's magnetic field constrained by the Io flux tube footprint, *J. Geophys. Res.*, **103**(A6), 11,929–11,940, doi:10.1029/97JA03726.
- Cowley, S. W. H. (1978), The effect of pressure anisotropy on the equilibrium structure of magnetic current sheets, *Planet. Space Sci.*, **26**(11), 1037–1061, doi:10.1016/0032-0633(78)90028-4.
- Cowley, S. W. H., and E. J. Bunce (2001), Origin of the main auroral oval in Jupiter's coupled magnetosphere-ionosphere system, *Planet. Space Sci.*, **49**, 1067–1088.
- Cowley, S. W. H., and E. J. Bunce (2003), Modulation of Jovian middle magnetosphere currents and auroral precipitation by solar wind-induced compressions and expansions of the magnetosphere: Initial response and steady state, *Planet. Space Sci.*, **51**, 31–56.
- Cowley, S. W. H., J. D. Nichols, and E. J. Bunce (2002), Distributions of current and auroral precipitation in Jupiter's middle magnetosphere computed from steady-state Hill-Pontius angular velocity profiles: Solutions for current sheet and dipole magnetic field models, *Planet. Space Sci.*, **50**, 717–734.
- Cowley, S. W. H., J. D. Nichols, and D. J. Andrews (2007), Modulation of Jupiter's plasma flow, polar currents, and auroral precipitation by solar wind-induced compressions and expansions of the magnetosphere: A simple theoretical model, *Ann. Geophys.*, **25**, 1433–1463.
- Delamere, P. A., A. Otto, X. Ma, F. Bagenal, and R. J. Wilson (2015), Magnetic flux circulation in the rotationally driven giant magnetospheres, *J. Geophys. Res. Space Physics*, **120**, 4229–4245, doi:10.1002/2015JA021036.
- Frank, L. A., and W. R. Paterson (2004), Plasmas observed near local noon in Jupiter's magnetosphere with the Galileo spacecraft, *J. Geophys. Res.*, **109**, A11217, doi:10.1029/2002JA009795.
- Frank, L. A., W. R. Paterson, and K. K. Khurana (2002), Observations of thermal plasmas in Jupiter's magnetotail, *J. Geophys. Res.*, **107**(A1), 1003, doi:10.1029/2001JA000077.

- Grodent, D., J. T. Clarke, J. Kim, J. H. Waite Jr., and S. W. H. Cowley (2003a), Jupiter's main auroral oval observed with HST-STIS, *J. Geophys. Res.*, **108**(A11), 1389, doi:10.1029/2003JA009921.
- Grodent, D., J. T. Clarke, J. H. Waite Jr., S. W. H. Cowley, J.-C. Gérard, and J. Kim (2003b), Jupiter's polar auroral emissions, *J. Geophys. Res.*, **108**(A10), 1366, doi:10.1029/2003JA010017.
- Grodent, D., J.-C. Gérard, A. Radioti, B. Bonfond, and A. Saglam (2008), Jupiter's changing auroral location, *J. Geophys. Res.*, **113**, A01206, doi:10.1029/2007JA012601.
- Hill, T. W. (1979), Inertial limit on corotation, *J. Geophys. Res.*, **84**(A11), 6554–6558, doi:10.1029/JA084ia11p06554.
- Hill, T. W. (2001), The Jovian auroral oval, *J. Geophys. Res.*, **106**(A5), 8101–8108, doi:10.1029/2000JA000302.
- Huang, T. S., and T. W. Hill (1989), Corotation lag of the Jovian atmosphere, ionosphere, and magnetosphere, *J. Geophys. Res.*, **94**(A4), 3761–3765, doi:10.1029/JA094ia04p03761.
- Jones, E., et al. (2001), SciPy: Open Source Scientific Tools for Python. [Available at <http://www.scipy.org/>, online; accessed 2015-12-01.]
- Kane, M., B. H. Mauk, E. P. Keath, and S. M. Krimigis (1995), Hot ions in Jupiter's magnetodisc: A model for Voyager 2 low-energy charged particle measurements, *J. Geophys. Res.*, **100**(A10), 19,473–19,486, doi:10.1029/95JA00793.
- Khurana, K. K., and M. G. Kivelson (1993), Inference of the angular velocity of plasma in the Jovian magnetosphere from the sweepback of magnetic field, *J. Geophys. Res.*, **98**(A1), 67–79, doi:10.1029/92JA01890.
- Khurana, K. K., M. G. Kivelson, V. M. Vasyliūnas, N. Krupp, J. Woch, A. Lagg, B. H. Mauk, and W. S. Kurth (2004), The configuration of Jupiter's magnetosphere, in *Jupiter: The Planet, Satellites and Magnetosphere*, edited by F. Bagenal, T. E. Dowling, and W. B. McKinnon, pp. 593–616, Cambridge Univ. Press, New York.
- Kivelson, M. G. (2015), Planetary magnetodiscs: Some unanswered questions, *Space Sci. Rev.*, **187**, 5–21, doi:10.1007/s11214-014-0046-6.
- Kivelson, M. G., and D. J. Southwood (2005), Dynamical consequences of two modes of centrifugal instability in Jupiter's outer magnetosphere, *J. Geophys. Res.*, **110**, A12209, doi:10.1029/2005JA011176.
- Krimigis, S. M., J. F. Carbary, E. P. Keath, C. O. Bostrom, W. I. Axford, G. Gloeckler, L. J. Lanzerotti, and T. P. Armstrong (1981), Characteristics of hot plasma in the Jovian magnetosphere—Results from the Voyager spacecraft, *J. Geophys. Res.*, **86**(A10), 8227–8257, doi:10.1029/JA086ia10p08227.
- Krupp, N., A. Lagg, S. Livi, B. Wilken, J. Woch, E. C. Roelof, and D. J. Williams (2001), Global flows of energetic ions in Jupiter's equatorial plane: First-order approximation, *J. Geophys. Res.*, **106**(A11), 26,017–26,032, doi:10.1029/2000JA900138.
- Krupp, N., V. M. Vasyliūnas, J. Woch, and A. Lagg (2004), Dynamics of the Jovian magnetosphere, in *Jupiter: The Planet, Satellites and Magnetosphere*, edited by F. Bagenal, T. E. Dowling, and W. B. McKinnon, pp. 617–638, Cambridge Univ. Press, Cambridge, U. K.
- Louarn, P., C. P. Paranicas, and W. S. Kurth (2014), Global magnetodisk disturbances and energetic particle injections at Jupiter, *J. Geophys. Res. Space Physics*, **119**, 4495–4511, doi:10.1002/2014JA019846.
- Mauk, B. H., and S. M. Krimigis (1987), Radial force balance within Jupiter's dayside magnetosphere, *J. Geophys. Res.*, **92**(A9), 9931–9941, doi:10.1029/JA092ia09p09931.
- Mauk, B. H., D. J. Williams, R. W. McEntire, K. K. Khurana, and J. G. Roederer (1999), Storm-like dynamics of Jupiter's inner and middle magnetosphere, *J. Geophys. Res.*, **104**(A10), 22,759–22,778, doi:10.1029/1999JA900097.
- McNutt, R. L. (1984), Force balance in outer planet magnetospheres, in *Physics of Space Plasmas, Proceedings of the 1982-4 MIT Symposia. SPI Conf. Proc. and Reprint Ser.*, edited by J. Belcher et al., pp. 179–210, Scientific, Cambridge, Mass.
- McNutt, R. L., J. W. Belcher, and H. S. Bridge (1981), Positive-ion observations in the middle magnetosphere of Jupiter, *J. Geophys. Res.*, **86**(A10), 8319–8342, doi:10.1029/JA086ia10p08319.
- McNutt, R. L., P. S. Coppi, and R. S. Selesnick (1987), Plasma depletions in the Jovian magnetosphere: Evidence of transport and solar wind interaction, *J. Geophys. Res.*, **92**, 4377–4398, doi:10.1029/JA092ia05p04377.
- Millward, G., S. Miller, T. S. Stallard, N. Achilleos, and A. D. Aylward (2005), On the dynamics of the Jovian ionosphere and thermosphere, *Icarus*, **173**(1), 200–211, doi:10.1016/j.icarus.2004.07.027.
- Nichols, J. D. (2011), Magnetosphere-ionosphere coupling in Jupiter's middle magnetosphere: Computations including a self-consistent current sheet magnetic field model, *J. Geophys. Res.*, **116**, A10232, doi:10.1029/2011JA016922.
- Nichols, J. D., and S. W. H. Cowley (2003), Magnetosphere-ionosphere coupling currents in Jupiter's middle magnetosphere: Dependence on the effective ionospheric Pedersen conductivity and iogenic plasma mass outflow rate, *Ann. Geophys.*, **21**, 1419–1441.
- Nichols, J. D., and S. W. H. Cowley (2004), Magnetosphere-ionosphere coupling currents in Jupiter's middle magnetosphere: Effect of precipitation-induced enhancement of the ionospheric Pedersen conductivity, *Ann. Geophys.*, **22**, 1799–1827.
- Nichols, J. D., and S. W. H. Cowley (2005), Magnetosphere-ionosphere coupling currents in Jupiter's middle magnetosphere: Effect of magnetosphere-ionosphere decoupling by field-aligned auroral voltages, *Ann. Geophys.*, **23**, 799–808.
- Nichols, J. D., J. T. Clarke, J.-C. Gérard, D. Grodent, and K. C. Hansen (2009), Variation of different components of Jupiter's auroral emission, *J. Geophys. Res.*, **114**, A06210, doi:10.1029/2009JA014051.
- Paranicas, C. P., B. H. Mauk, and S. M. Krimigis (1991), Pressure anisotropy and radial stress balance in the Jovian neutral sheet, *J. Geophys. Res.*, **96**(A12), 21,135–21,140, doi:10.1029/91JA01647.
- Pontius, D. H., Jr. (1997), Radial mass transport and rotational dynamics, *J. Geophys. Res.*, **102**(A4), 7137–7150, doi:10.1029/97JA00289.
- Ray, L. C., R. E. Ergun, P. A. Delamere, and F. Bagenal (2010), Magnetosphere-ionosphere coupling at Jupiter: Effect of field-aligned potentials on angular momentum transport, *J. Geophys. Res.*, **115**, A09211, doi:10.1029/2010JA015423.
- Ray, L. C., N. A. Achilleos, M. F. Vogt, and J. N. Yates (2014), Local time variations in Jupiter's magnetosphere-ionosphere coupling system, *J. Geophys. Res. Space Physics*, **119**, 4740–4751, doi:10.1002/2014JA019941.
- Siscoe, G. L., and D. Summers (1981), Centrifugally driven diffusion of iogenic plasma, *J. Geophys. Res.*, **86**(A10), 8471–8479, doi:10.1029/JA086ia10p08471.
- Smith, C., and A. D. Aylward (2009), Coupled rotational dynamics of Jupiter's thermosphere and magnetosphere, *Ann. Geophys.*, **27**(1), 199–230, doi:10.5194/angeo-27-199-2009.
- Southwood, D. J., and M. G. Kivelson (2001), A new perspective concerning the influence of the solar wind on the Jovian magnetosphere, *J. Geophys. Res.*, **106**(A4), 6123–6130, doi:10.1029/2000JA000236.
- Tao, C., H. Fujiwara, and Y. Kasaba (2009), Neutral wind control of the Jovian magnetosphere-ionosphere current system, *J. Geophys. Res.*, **114**, A08307, doi:10.1029/2008JA013966.
- Tao, C., H. Fujiwara, and Y. Kasaba (2010), Jovian magnetosphere-ionosphere current system characterized by diurnal variation of ionospheric conductance, *Planet. Space Sci.*, **58**(3), 351–364, doi:10.1016/j.pss.2009.10.005.

- Vasyliūnas, V. M. (1983), Plasma distribution and flow, in *Physics of the Jovian Magnetosphere*, edited by A. J. Dessler, pp. 395–453, Cambridge Univ. Press, Cambridge, U. K., doi:10.1017/cbo9780511564574.013.
- Vogt, M. F., M. G. Kivelson, K. K. Khurana, R. J. Walker, B. Bonfond, D. Grodent, and A. Radioti (2011), Improved mapping of Jupiter's auroral features to magnetospheric sources, *J. Geophys. Res.*, *116*, A03220, doi:10.1029/2010JA016148.
- Vogt, M. F., M. G. Kivelson, K. K. Khurana, R. J. Walker, M. Ashour-Abdalla, and E. J. Bunce (2014), Simulating the effect of centrifugal forces in Jupiter's magnetosphere, *J. Geophys. Res. Space Physics*, *119*, 1925–1950, doi:10.1002/2013JA019381.
- Yates, J. N., N. Achilleos, and P. Guio (2012), Influence of upstream solar wind on thermospheric flows at Jupiter, *Planet. Space Sci.*, *61*(1), 15–31, doi:10.1016/j.pss.2011.08.007.